Two-Point Focused Laser Differential Interferometry Second-Mode Measurements at Mach 6

Joshua M. Weisberger*, Brett F. Bathel†, Gregory C. Herring‡, Rudolph A. King§, Amanda Chou¶, and Stephen B. Jones‖
NASA Langley Research Center, Hampton, VA, 23606

A two-point focused laser differential interferometer (FLDI) is used to make measurements of density fluctuations on a 7 degree half-angle cone in a Mach 6 flow. The system was first characterized in the laboratory using laser induced breakdown to provide a well defined density fluctuation. The speed of the shock wave generated by the breakdown is verified using simultaneous high-speed schlieren. The FLDI system is then installed at the NASA Langley 20-Inch Mach 6 air tunnel to make measurements in the boundary layer of the 7 degree half-angle cone model and in the tunnel freestream for a unit Reynolds number range of 3.0 to 8.22×10^6 ft^{-1}. Second-mode packets are visible in the spectra, with peak frequencies increasing linearly and peak amplitude increasing as a function of unit Reynolds number. The two-point measurement allows for the calculation of the second-mode wavepacket speeds, which propagate between 88% and 92% of the freestream velocity of the tunnel for all Reynolds numbers. The FLDI measurements are compared to surface-mounted fast-response pressure transducer measurements, where second-mode frequencies and wavepacket speeds are in good agreement.

I. Introduction

The design and development of hypervelocity flight vehicles relies heavily on knowledge of the location of transition from laminar to turbulent flow, due to an increase in both friction and surface heating rates when flow transitions. Without adequate knowledge of transition locations, larger thermal protection systems must be used, increasing the vehicle's weight and significantly changing structural designs. Ground test facilities are invaluable for gaining an understanding of the underlying physics of the transition process, where simplified test article geometries allow for continuity and comparison of results over a range of different facilities. A cone at zero angle of attack is a common geometry for boundary layer transition testing [1]. With ground test facilities comes another challenge: the freestream environment. This freestream environment differs from the actual flight freestream environment, so its characterization has been the subject of many studies, including the influence of the freestream on the boundary layer transition process (boundary layer receptivity). In hypervelocity boundary layers, the acoustic instability is the dominant transition mechanism derived by Mack in the early 1970s, and is termed the "second-mode" instability [2, 3].

Numerous experimental methods of measuring both freestream disturbances and boundary layer transition have been used in ground test facilities. One of the first measurements of the freestream disturbance used a hot-wire [4], and hot-wire measurements were also used to measure transition on a slender, sharp cone [5]. Tanner described the use of interferometric optical techniques for use in fluid flows [6]. Piezo-electric pressure transducers have been used more recently, in both a pitot orientation for freestream disturbance measurements [7] and in flush surface-mounted configurations for surface transition measurements [8, 9]. The viable frequency range for these PCB sensors ranges from paper to paper, but a recently published conference paper provides greater insight into the limits of the probe at higher frequency [10].

In the early 1970s, Smeets [11–13] and Smeets and George [14] used both a laser differential interferometer (LDI) and focused laser differential interferometer (FLDI) system for various fluid dynamics problems These systems measure small density fluctuations at high frequencies, above frequencies other techniques such as hot wire probes and surface

*Research Engineer, Advanced Measurements and Data Systems Branch, AIAA Student Member.
†Research Engineer, Advanced Measurements and Data Systems Branch, AIAA Senior Member.
‡Research Physicist, Advanced Measurements and Data Systems Branch.
§Research Aerospace Engineer, Flow Physics and Control Branch, AIAA Member.
¶Research Aerospace Engineer, Flow Physics and Control Branch, AIAA Senior Member.
‖Research Technician, Analytical Mechanics Associates.

mounted piezo-electric sensors are sensitive to. The LDI and FLDI techniques use two closely-spaced, orthogonally polarized beams to measure the change in their relative phase due to density gradients along their path through a fluid of interest. A similar technique to LDI has been used, but this time with reflected/scattered light from a model (that could be used with more complex model geometries) to measure transition in a transonic wind tunnel [15]. Advancements in data acquisition technology have reinvigorated the drive to use this technique for high-speed flow measurements, since it is both non-intrusive and relatively insensitive to facility vibrations. Recently, ongoing research has been focused on the simulation [16, 17], characterization [18], and implementation of the system. Freestream disturbance level measurements in ground test facilities has been studied [19–23], with emphasis in some studies on the effect of shock-tube cleanliness on the disturbance levels [21, 22]. Instability measurements have also been performed in the boundary layer of either a test model or on the tunnel walls of a test facility [21, 22, 24–27].

A drawback of the single-point FLDI system is that evolution of the measured phenomena of interest (second-mode packets for example) cannot be observed; a measurement is made at a single location, and no information downstream is known. This is currently where surface flush-mounted probes can provide extra information where non-intrusive optical measurements may be lacking. For example, in the testing campaign that is the subject of this paper, more than 20 surface probes were used, at locations from the nose tip to the cone base and around multiple cone rays. Two-point FLDI has the ability to begin to bridge this gap, to allow a non-intrusive probe to measure disturbance evolution. Smeets recognized the need for multiple simultaneous measurements and performed an eight-beam LDI measurement on a cone boundary layer [12]. Parziale *et al.* used two separate FLDI instruments to make measurements of disturbance propagation in a hypervelocity boundary layer with a separation distance of approximately 91 mm [24–26]. Further improvement of the two-point FLDI system was performed by Jewell et al. with the use of a microscope slide to obtain two point-measurements located approximately 1000 μm away from each other [27]. These measurements were made in a small shock tube, and second-mode packets were observed. Most recently, two-point FLDI systems were used to make measurements of phase speeds/velocities of disturbances in a turbulent jet [28, 29].

This study has three aims: provide a detailed experimental setup overview for a two-point FLDI system, validate the results of the two-point system in the laboratory with a laser induced breakdown spark test, and utilize the system for both freestream and boundary layer transition measurements on a 7 degree half-angle cone (second-mode wavepackets and turbulent spots) at the NASA Langley 20 Inch Mach 6 Air Tunnel. In Section II, the experimental setup for both the laboratory spark test and the 20 Inch Mach 6 test are detailed. In Section III, the methods for aligning the FLDI system are extensively reviewed. A method for alignment without access to the test section provides a novel way to increase the up-time of the system, which is useful for quick turnaround facilities such as the 20 Inch Mach 6. In Section IV, the results of the laboratory laser induced breakdown spark tests are discussed. These tests are used to validate the phase speed measurement capability of the two point system in various orientations, using a well defined, repeatable disturbance. A high-speed schlieren system is used to compare to the FLDI results. In Section V, results from both the two-point FLDI system and two piezoelectric pressure transducers in close proximity to the FLDI measurement location are discussed for a 7 degree half-angle cone model in a Mach 6 flow. Results include freestream measurements and their run-to-run repeatability, identification of four types of flow features observed in the cone boundary layer, second-mode packet time duration and propagation velocities, and finally a comparison of a second-mode packet between closely spaced FLDI and pressure transducer measurements.

II. Experimental Setup

The FLDI system comprises two independent breadboards, termed the "pitch" and "catch" boards. With appropriate spacing of the two boards, a density disturbance can be measured at the point of focus between them. A schematic of the FLDI system is shown in Fig. 1. The superscripts P and C denote the pitch and catch boards, respectively, while the numbers preceding the letters in the superscripts denote the instance of identical components along the beam path. Specific vendor and manufacturer names are explicitly mentioned only to accurately describe the test hardware. The use of vendor and manufacturer names does not imply endorsement by the U.S. Government, nor does it imply that the specified equipment is the best available. On the pitch board (consisting of legs L1, L2, and L3), a laser (L) emits linearly polarized light at 532 nm, and includes a physical aperture (A) to block emission without turning off the laser. A shutter (S) and its controller (KC) is connected to the interlock system of either the laboratory or the ground test facility to ensure the laser only passes through the system when qualified operators are present. Two mirrors (M^{1P} and M^{2P}) are used to align the beam directly along the optical axis of the system. A half-waveplate (HWP^{1P}) coupled with a polarizing beamsplitter cube (PBS) is used to adjust the transmitted power of the laser through the system. Horizontally polarized light is diverted into the beam dump (BD), while vertically polarized light is allowed to pass through. A

second half-waveplate (HWP^{2P}) is used to rotate the linearly polarized light from the PBS, which is then expanded through a beam expander (BE) and is split into two separate beams by a polarizing Nomarski prism (NP). The rotation of the HWP^{2P} is set relative to the orientation of the NP such that the beam is split into two beams of equal intensity. These output beams are linearly polarized (and orthogonal to each other), and the rotation of a third half-waveplate (HWP^{3P}) is set relative to the orientation of a Wollaston prism (W^{P}), which splits each beam again into two orthogonal, linearly polarized beams. There are two significant benefits of using the NP:

1) Because the two beams from the NP converge at the W^{P}, the two beams propagate parallel to each other in the test section.
2) The convergence axis of the NP is aligned with the optical axis of the system. This means the NP can be placed in a simple rotation mount to orient the beams in any orientation. If a Koester prism were to be used instead [12], it would need a more complicated mounting to enable full rotation because the axis of splitting is not aligned with the optical axis of the system.

Two achromatic doublets (FL^{1P} and FL^{2P}) are used to first collimate and then focus the expanding beams down to a point in the test section (TS) at the focal distance of FL^{2P}, which for this system was 750 mm. This value was chosen to allow for adequate room to position the FLDI system straddling the 20 Inch Mach 6 tunnel. FL^{P} denotes the equivalent optic created from the back-to-back placement of FL^{1P} and FL^{2P}. The TS leg in the schematic will be used in this paper to denote the section between the two breadboards (between FL^{2P} and FL^{1C}).

Two types of beam polarization splitting occur in the system. The first is through the Nomarski prism, and the two resulting beams will be called the Nomarski prism pair (NP-pair). Each of these NP-pair beams is then split again through the Wollaston prism, and these two resulting beams will be called the Wollaston pair (W-pair). That is, for each NP-pair beam, there is a W-pair. The NP-pair creates two separate measurement points in the flow field (equivalent to two FLDI instruments) while the W-pair provides sensitivity to density fluctuations.

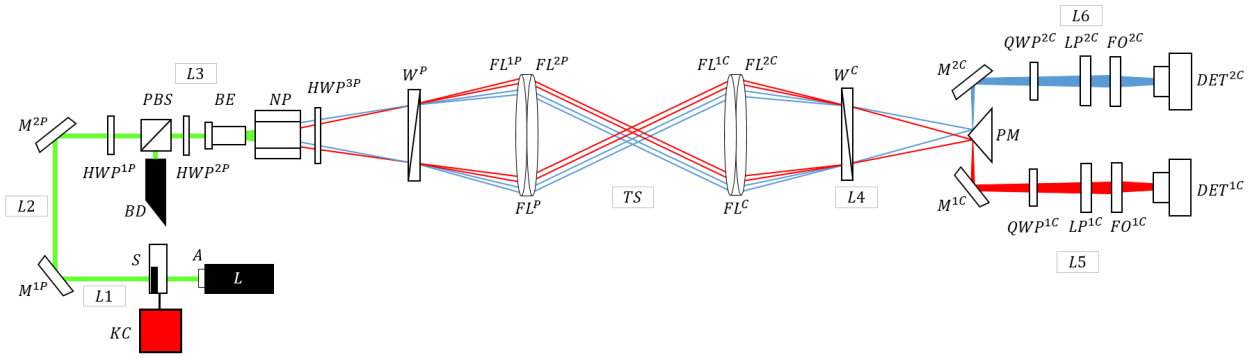

Fig. 1 Schematic of the two-point FLDI setup. The laser emits at 532 nm, and is displayed with a green line. The blue and red colors each correspond to a Nomarski-pair beam (but do not indicate a change in wavelength).

The catch breadboard consists of legs L4, L5, and L6. The two NP-pair beams expand past the focus in the test section and are collimated and focused using a matching achromatic doublet (FL^{1C} and FL^{2C}, forming the equivalent FL^{C}). The W-pair beams are recombined using a matching Wollaston prism (W^{C}), and the two separate NP-pair beams continue to focus. The beams are split into their respective legs using a right angle prism mirror (PM), and both L5 and L6 contain identical components. First, a mirror (M^{1C} or M^{2C}) is used to both fold the beam path to keep the system compact, and to provide angular adjustment onto the detector face. The beam then passes through a quarter-waveplate (QWP^{1C} or QWP^{2C}) to adjust the polarization state of the beam. A linear polarizer (LP^{1C} or LP^{2C}) is then used to ensure the system operates at the middle (linear region) of the interference fringe. Finally, a focusing optic (FO^{1C} or FO^{2C}) is used to focus the beam to the correct spot size on the detector (DET^{1C} or DET^{2C}). Correctly focusing the beam on the detector element is important for high frequency response, and is discussed in Section III.E.

Using a 3D-printed NP mount threaded into a cage rotation mount (CRM1, Thorlabs), the NP-pair can be rotated to any orientation. To account for the NP-pair orientation on the catch side, the PM and legs L5 and L6 are mounted to the 30 mm fixed cage using a rotating cage segment plate (CPR1, Thorlabs). This allows the PM-L5-L6 subsystem to be rotated easily and fixed in place for measurements.

Table 1 Components and part numbers used in the current setup.

Symbol	Company	Part Number	Symbol	Company	Part Number
L	Thorlabs	532-300-CDRH	NP	United Crystals	-
S	Thorlabs	SH1	W	United Crystals	-
KC	Thorlabs	KSC101	FL	Newport	PAC097AR.14
HWP	Newport	10RP02-16	PM	Thorlabs	MRA25-G01
QWP	Thorlabs	WPQ10M-532	LP	Thorlabs	LPVISA100-MP2
PBS	Newport	CCM1-PBS25-532	FO	Thorlabs	LB1811-A-ML
BD	Thorlabs	BT610	DET	Thorlabs	DET100A2
BE	Thorlabs	TRH127-020-A-ML	M	Newport	10D20DM.11

Table 2 Optical properties of FLDI components.

Name	Symbol	Value	Units	Notes
Laser wavelength	λ	532	nm	-
Wollaston splitting angle	σ	2	arcmin	-
Focal length FL^{1P}	f_{1P}	750	mm	-
Focal length FL^{2P}	f_{2P}	750	mm	-
Field lens diameter	$D_{4\sigma}$	50.8	mm	-
Field lens EFL	f_e	375	mm	Eq. (1)
W-pair separation	Δx_{W}	218.2	μm	Eq. (2)
Beam waist diameter	w_0	5.0	μm	Eq. (3)
NP-pair separation	Δx_{NP}	2.473	mm	Section II.D

In Table 2, the setup-specific components and optical properties can be found. The effective focal length of the achromatic doublet is found using Eq. (1), which governs the location of the W^P because the W-pairs must travel parallel through the test section. This value is the same for both the pitch and catch sides because the field lenses are identical.

$$f_{\mathrm{e}} = \left(\frac{1}{f_{1P}} + \frac{1}{f_{2P}}\right)^{-1} = 375 \text{ mm} \tag{1}$$

The theoretical beam separation at the focus due to the W^P splitting is calculated using the effective focal length and the Wollaston splitting angle in Eq. 2.

$$\Delta x_{\mathrm{W}} = 2 f_{\mathrm{e}} \tan\left(\frac{1}{2}\frac{\sigma}{60}\right) = 218.2\ \mu m \tag{2}$$

The theoretical beam waist diameter is found from Eq. 3, using the wavelength of the laser, the focal length of the field lens, and the 4σ diameter of the field lens. Later measurements with a CMOS camera show a beam waist approximately four times the calculated beam waist diameter. This is due to the added optics along the beam path between the BE and FL^P. When these components are removed, the beam waist diameter measured at the focus closely matches the theoretical beam waist diameter.

$$w_0 = \frac{2\lambda f_{1P}}{\pi D_{4\sigma}} = 5.0\ \mu m \tag{3}$$

The convergence angle of the NP is found experimentally in Section II.D. The laser power was measured using a Vega power meter (Ophir) with a PD300-3W sensor head. A 10-bit monochrome camera (Edmund Optics, EO-23121M) was used for alignment purposes both at the test section focus and at the catch side focus. The camera has 5.86 μm square pixels and both a 550 nm long-pass filter (Thorlabs, FGL550M) and an OD 6 neutral density filter (Thorlabs, NE60A-A)

placed in front of the sensor to better image the beam pair. For the spark tests, a Basler ace camera (acA2040-120um) with higher resolution (2048 × 1536 pixels with pixel pitch of 3.45 μm) was used instead.

A. Laser Induced Breakdown Spark Test

The sensitivity of the two-point FLDI system and its ability to accurately determine the phase speed of a disturbance is investigated using a wave generated by laser induced breakdown (LIB). The FLDI system was set up in conjunction with a high-speed schlieren (HSS) system and a high-power laser to measure the wave speed of a blast generated from laser induced breakdown. A top view schematic of the three-subsystem setup is shown in Fig. 2a. The optical axes of the FLDI and HSS subsystems are orthogonal. The FLDI beam focus is located at the center of the field of view (FoV) of the HSS. A flat aluminum reflection plate was placed 65.3 mm below the FLDI beam focus. The LIB laser system was oriented at an oblique angle to the axes of the FLDI and HSS, as this was most convenient given space on the optical table. Its optical axis was 66.7 mm above the FLDI beam focus.

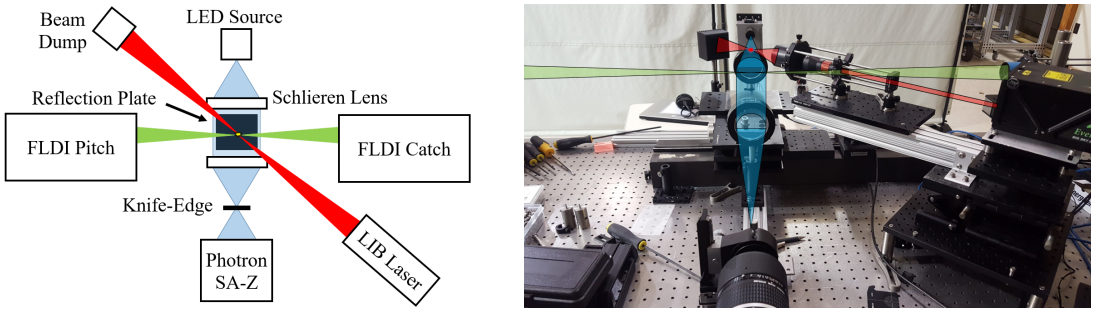

(a) **(b)**

Fig. 2 Spark test (a) schematic top-view and (b) picture from behind schlieren camera (Photron SA-Z), with light beams shown in green (FLDI), blue (HSS) and red (LIB).

The HSS system consists of a high speed LED source, two 75 mm diameter, 400 mm focal length achromats, a knife-edge in a three-axis translation stage, and a high-speed Photron SA-Z camera. The LIB laser (EverGreen, Quantel) is a dual pulsed (for PIV) Nd:YAG laser emitting at 532 nm, and is operated in Q-switched mode to attain energies of approximately 219 mJ per pulse. Breakdown was induced at lower energies, but the largest possible energy of the laser was used to attain the strongest spark possible. A high-power beam expander (BE030-532, Thorlabs) increases the size of the beam diameter from 7 mm to 21 mm. A lens with a focal length of 100 mm focuses the beam down to a spot to induce breakdown. A beam dump (LB2, Thorlabs) was placed along the beam axis after the breakdown to safely dump the excess light. The nine test cases (NP-pair and W-pair orientations) are shown in Fig. 3a, where the wave from the LIB travels from top to bottom in each frame. Images from a CMOS camera were acquired at the test section focus during alignment for each spark test case, and can be seen in Fig. 3b.

A BNC Model 577 (4-channel) digital delay/pulse generator was used for triggering the LED, SA-Z, EverGreen, and the FLDI system. The main system clock pulse output was set to 200 kHz. One channel controlled when the camera was triggered, and was synced to the system clock so it always ran at 200 kHz. Another channel controlled the LED triggering indirectly through the camera software. Since the spark was located 66.7 mm above the FLDI beam focus, the wave took $\approx$ 0.275 ms to reach the top of the schlieren FoV, so the HSS acquisition was delayed until just before the shock entered the FoV. A third channel triggered the EverGreen laser and the FLDI scope. The full frame size of the camera sensor is 1024 × 1024, but in order to run at 200 kHz, the FoV was cropped to 128 × 320. The oscilloscope (Tektronix MSO6) was used to acquire a data set at every trigger, ensuring accurate correlation between the schlieren sequence and the FLDI time record. Two insulated 6 ft 50 Ω BNC cables (L-Com, CCTN5806B) terminated at 50 Ω were connected to the photodiodes, and the sampling rate was 250 MHz with a record length of 250 MS.

B. 20-Inch Mach 6 Setup

The FLDI system was installed at the NASA Langley 20-Inch Mach 6 air tunnel to measure both freestream disturbances and boundary layer instabilities on a 7 degree half-angle cone. The small footprint of the FLDI system allowed measurements to be made simultaneously with a HSS system (not co-linear), even though the tunnel windows

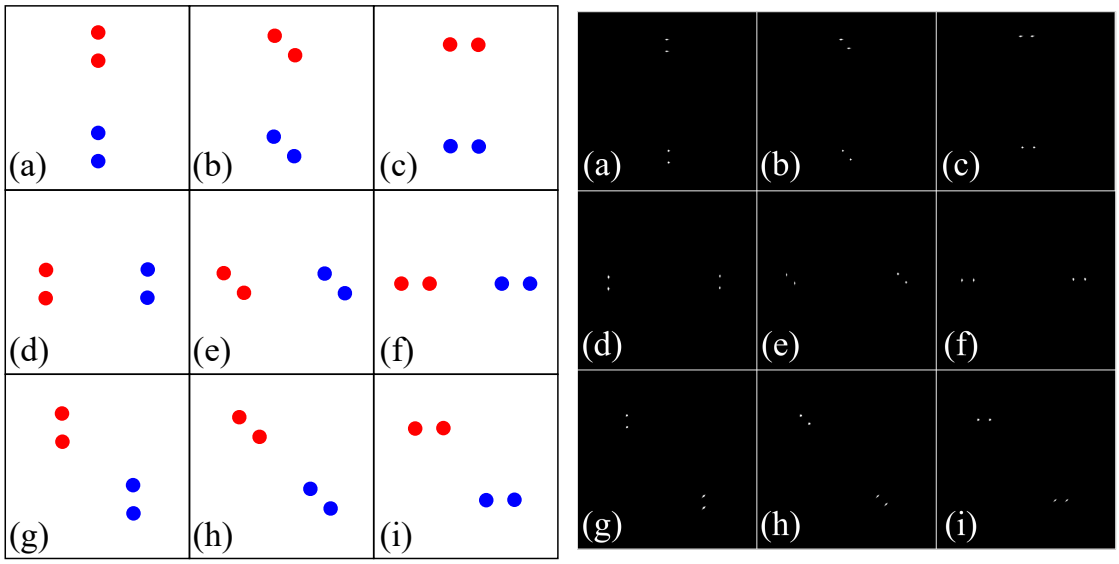

(a) **(b)**

Fig. 3 Matrix of (a) the schematic of spark test NP-pair and W-pair orientations, and (b) the corresponding CMOS images of orientations. In each sub-figure, (a-c) denotes vertical NP-pairs, (d-f) denotes horizontal NP-pairs, and (g-i) denotes 45° **NP-pairs. W-pair orientations are (a,d,g) vertical, (b,e,h)** 45°**, and (c,f,i) horizontal.**

are only 43.2 cm in diameter. Pictures of the pitch and catch sides installed at the facility can be seen in Figs. 4a and 4b, respectively. Note that the model is not injected for these images, so the view through the tunnel windows is clear. A Tektronix oscilloscope (3.5 GHz) was used for acquisition. The sampling rate over the course of the testing campaign was 10 MHz, the record length was 20 MS (for a sampling time of 2 sec), the horizontal resolution was 200 mV/div, the vertical resolution was 10 mV/div, and the termination was 50 Ω (smaller signal but higher frequency response).

Space was limited at the test section of the 20-Inch Mach 6 tunnel, so decisions about where to locate electronics and data acquisition equipment were partially dictated by these limitations (space and safety). Alignment of the system took place on both the pitch and catch sides of the tunnel, and visibility over the tunnel was poor, so both sides were required to have a linked monitor. Both scopes and the computer tower were located on the catch side of the tunnel, and a KVM extender was used to extend visibility and control to the pitch side. For safety reasons, operators were not allowed outside the control room during runs, so another KVM extender provided control of the acquisition system and cameras down in the control room, where system arming and saving of the data was controlled. One CMOS camera was placed on the pitch board for aligning the FLDI beams with the model surface. A second CMOS camera was used on the catch board to align the system when test section access was limited (detailed in the Appendix). A BNC Model 577 was used to trigger the acquisition systems, including the FLDI, the HSS, and the surface mounted sensors.

Four configurations of the W-pairs and NP-pairs were used during the testing campaign. A schematic of these configurations is shown in Fig. 5, where configuration A was used for runs 1 to 5, configuration B for runs 6 to 68, configuration C for runs 69 to 82, and configuration D for runs 82 to 93. Different nose tips were used throughout the tests, from a sharp tip (radius of 0.006 inches) to a blunt tip (radius of 0.5 inches). In Run 68, a turbulent trip was added near the cone nose tip to induce fully turbulent flow. For the majority of the runs, three data sets were acquired: one set while the tunnel was under vacuum before the run (called *OnSphere*), one set while the model was injected (called *ModelInjected*), and one set of the freestream flow after the model was retracted (called *Freestream*).

C. Full Setup Logistics

When using the FLDI system in ground test facilities (not just the laboratory), the logistics of movement and placement of the system is an important factor to take into consideration in the design. For the test in the 20 Inch Mach 6 facility, there were a number of requirements to be met:

1) The pitch and catch breadboards should be easily lifted by two people, and could be lifted by one person if

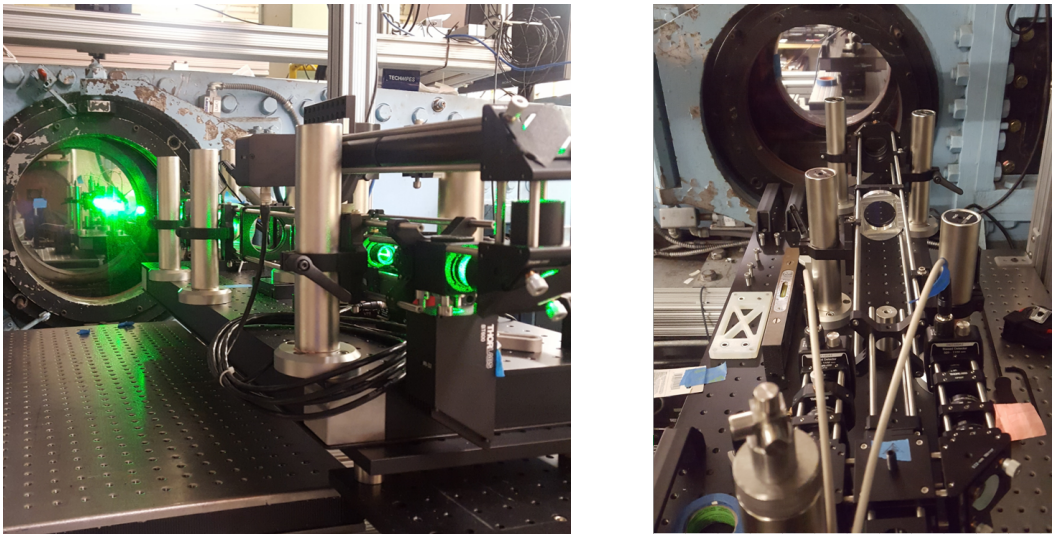

(a) **(b)**

Fig. 4 FLDI setup at the 20 Inch Mach 6 Air Tunnel showing the (a) pitch side (with laser on) and the (b) catch side (with laser off).

necessary. The weight of the optics themselves are negligible, but the breadboard and mounting hardware make up the bulk of the weight.

2) The entire pitch and catch breadboards should be positioned vertically with relative ease. The lightest (but still rigid) breadboards were used, and high-load Z-axis jacks with easily adjustable manual jack-screws were used.
3) The Z-axis jacks need enough travel to position the FLDI beams anywhere on the cone, from front (near to window centerline) to rear (up to 5 cm above window centerline).
4) The NP-pair must be easily adjusted to any orientation. Both the HWP^{2P} and NP were placed in rotation mounts. Because the NP-pair could rotate, the two detectors needed to be able to rotate as well. The entire PM-L5-L6 subsystem was mounted such that it could rotate relative to the fixed cage system to allow for the correct splitting of the NP-pair beams after the W-pair beams were recombined with the W^C.
5) The W-pair must be easily adjusted to any orientation. The solution was to mount both the upstream half-waveplate (HWP^{3P}) and the pitch and catch Wollaston prisms (W^C and W^P) in rotation mounts.
6) The entire pitch-catch system must be able to laterally translate with respect to the tunnel axis with ease, in order to position the beams at the correct position on the model. Both Z-axis jacks (which the breadboards are sitting on) were mounted to T-slotted aluminum rails which could be loosened and slid to the desired location.

D. Nomarski Pair Separation

The separation of the NP-pairs is important to know accurately for disturbance velocity calculations. For this system, the NP needed to have a small convergence angle (beams converge more slowly). The plane of crossing needs to be located at the W^P, which is located at the effective focal distance upstream of the FL^P (375 mm). The BE must be located at the upstream focal length of the FL^{1P} (750 mm). Because the clear aperture of the NP is small (2.54×2.54 cm), it must be located near the BE, and in order to have its crossing point be located at the W^P, the splitting angle must be smaller than normally used in its applications in differential interference contrast (DIC) microscopy. The small splitting angle also keeps the NP-pair separation distance small, and avoids overfilling of the FL^P by the diverging beams.

The collimated laser beam was used to find the NP convergence angle. A CMOS camera (pixel pitch of 5.86×5.86 μm) was placed at six different locations along the beam path post-NP. The distance of each image along the optical axis was measured from the exit plane of the NP: 6.99 cm, 10.8 cm, 14.6 cm, 33.0 cm, 41.2 cm, and 46.5 cm. Beam profiles from each location along the optical axis can be seen in Fig. 6. The dashed black line indicates the laser axis of propagation, oriented parallel and coincident with the optical axis (because the NP splits symmetrically about the optical axis). The peak locations for each beam profile are computed using a Gaussian fit about each beam profile peak,

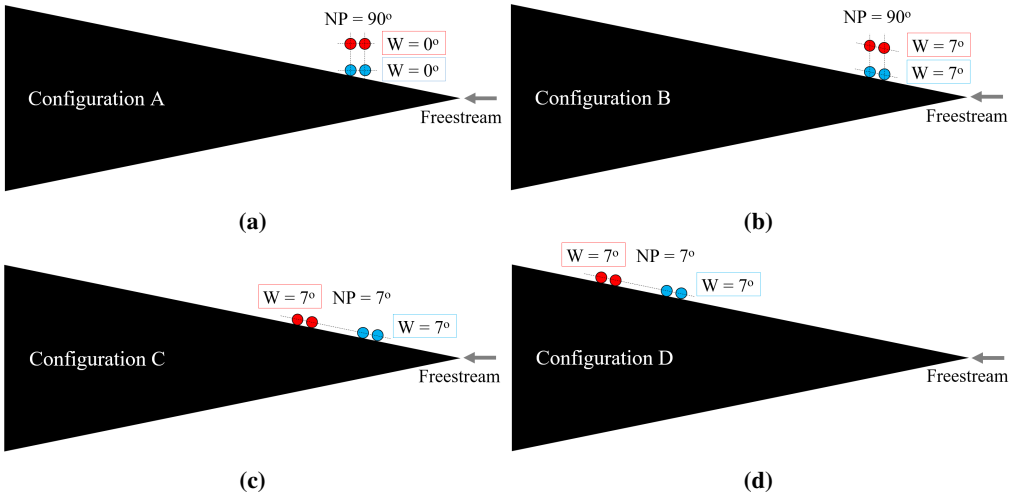

Fig. 5 Configuration and orientation for the FLDI setup for (a) runs 1 to 5, (b) runs 6 to 68, (c) runs 69 to 81, and (d) runs 82 to 93. All angles are with respect to the freestream velocity, and schematic is not to scale. Nose tip radius changed throughout the testing campaign.

and the locations are indicated with appropriately colored lines dropped down to the black circles (on the Z location of zero for clarity). The red dashed lines are the result of a linear regression through the peak points (the profile at 14.6 cm was not used in the regression calculation). The convergence half-angle between the red dashed lines and the optical axis is $\theta = 0.189°$. The crossing point distance from the NP exit plane is needed in order to place the NP at the correct distance away from the W^P. This was found by the intersection of the dashed red lines, and is located 267 mm from the the NP exit plane. Because the crossing point occurs at the W^P, which is located 375 mm from the FL^P, the theoretical separation of the NP-pair at the test section focus can be calculated using Eq. (4).

$$\Delta x_{\mathrm{NP}} = 2 f_e \tan(\theta) = 2\,(375\ mm) \tan(0.189°) = 2.47\ mm \tag{4}$$

E. Photodiodes

Two Thorlabs DET100A2 photodiodes are used in the system, each powered by a single 12 V A23 battery to keep noise from the power source low (keeps the power isolated from noisy line power). The quoted responsivity at 532 nm is $\mathcal{R} = 0.3228$ A/W. These photodiodes are current output devices, where the output is directly proportional to the amount of light incident on the detector. This current is then converted to a voltage (measured by the oscilloscope) by using a terminating load resistor. Speed of response for the FLDI measurements is imperative, so a low load resistance of 50 Ω is used, which has the added benefit of matching the impedance of the coaxial cables used to connect the photodiodes to the oscilloscope. For these experiments, the power of the laser was set to approximately 85 mW. When operating the two-point FLDI system, the power is split evenly between the two NP-pair beams, and the power incident on each detector is thus 30 mW (after optical losses through the components along the beam path). The photocurrent produced on each photodiode is shown in Eq. (5), which falls just below the maximum possible current for the detector (10 mA).

$$I_{\mathrm{current}} = \mathcal{R} P = (0.3228\ A/W)\,(30\ mW) = 9.68\ mA \tag{5}$$

The batteries generally have a rating of 55 mAh, resulting in a lifetime of ≈ 5.3 hours. This means the detectors can run continuously at the stated incident power for this duration. Lowering the power increases the lifetime, as does shutting off the detectors or shuttering the laser when not acquiring data. Monitoring the battery life is important in order to avoid losing signal during a run. Using a 50 Ω load resistance results in an output voltage of ≈ 484 mV (maximum possible 500 mV).

Photodiodes have an ideal linear operating range, where the output current is proportional to the incident power. While these detectors can in theory operate up to 10 mA (500 mV at 50 Ω load resistance), the relationship between current and power is no longer linear at these higher values. Neutral density (ND) filters were used to find the upper limit of the linear region of photodiode response. The voltage from the detector was measured with both an ND filter

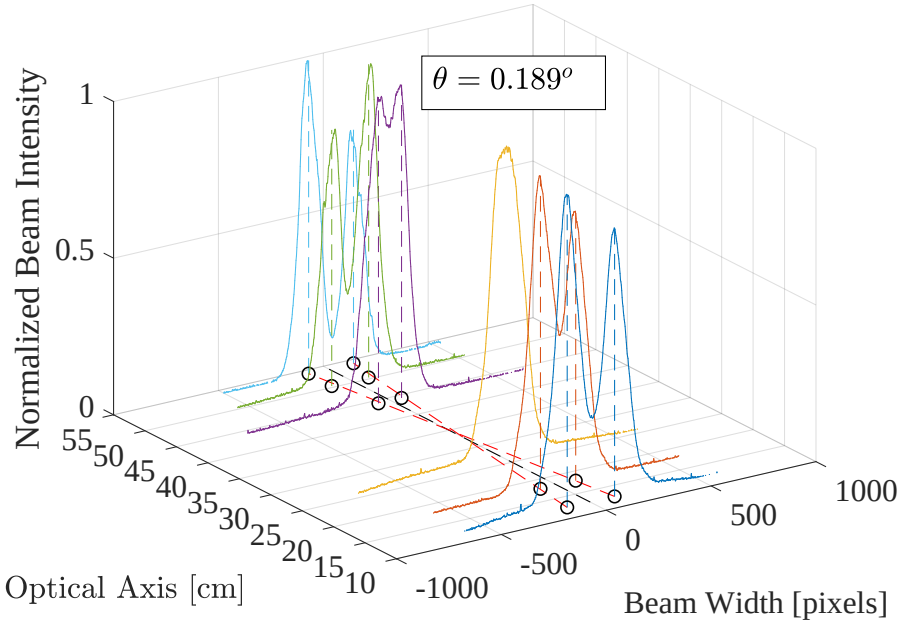

Fig. 6 Profiles of beam spots at different distances along the optical axis due to the NP divergence angle. Black dashed line indicates optical axis, and black circles indicate beam profile peak positions. Red dashed lines are linear regressions through the appropriate peak points.

inserted into the beam path and without the ND filter inserted. Both ND = 0.6 (ND6) and ND = 0.8 (ND8) filters were used in these tests. Measurements were recorded for laser power settings from its minimum up to its maximum value (300 mW) by rotating the HWP^{1P} ahead of the PBS. The resulting laser power was measured directly before the detector face. The lower limit of the photodiode linear range is not found because the laser power was not able to be attenuated low enough to find that limit. In Fig. 7a, voltage measured by the detector is plotted versus laser power. The voltage measured on the detector without either filter is shown with black squares, and the voltage measured with ND6 and ND8 filters in the beam path are plotted with red circles and blue triangles, respectively. The expected voltages are plotted with a dashed black line based on the detector's quoted responsivity at 532 nm of $\mathcal{R}$ = 0.3228 A/W.

For every power measured, the voltage with ND filter in place is divided by the voltage without the ND filter to obtain a normalized voltage that should be equal to the filter attenuation when the detector is operating in the linear region. To provide a clear indication of the extents of the linear region, the normalized voltage is plotted against the detector measured voltage in Fig. 7b. The deviation from linear response occurs near 450 mV, which corresponds to a power of approximately 35 mW. The red and blue dashed lines are the mean values of the normalized voltages for the linear range, which for the ND6 filter is 0.294 and for the ND8 filter is 0.162. These values are used to compute the actual filter attenuation, which for ND6 is 0.53 instead of 0.6, and for ND8 is 0.79 instead of 0.8. Using the known linear power range, the slope of the measured detector voltages in Fig. 7a (black squares and solid black line) is used to compute the detector's effective responsivity of 0.259 A/W, slightly lower than its quoted value.

F. System Transmission

Data was taken to assess the amount of attenuation of the laser through the optics, which have anti-reflection coatings wherever possible. The power meter was used to take measurements at points along the beam path where the entire beam could fit on the measurement head. The power measured before the BE was 110.2 mW, at the TS focus was 71.0 mW, just before the PM was 64.1 mW, and before the detector was 18.7 mW. The transmission of each component can be computed from these power measurements in addition to some known values. The transmission through the W^{P}, FL^{1P}, and FL^{2P} is found in Eq. (6).

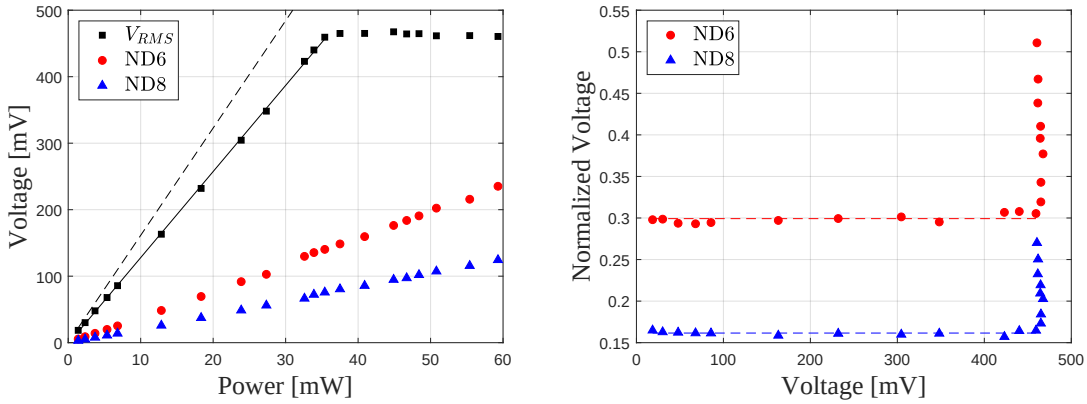

Fig. 7 Photodiode DC saturation data for (a) voltage versus power and (b) normalized voltage versus measured voltage. The solid black line is a linear fit to the linear range of data, and the dashed black line is calculated from the manufacturer's stated responsivity, using a 50 Ω load resistance.

$$\mathcal{T}_{\text{FL-FL-W}} = \frac{64.1\text{ mW}}{71.0\text{ mW}} = 90.28\% \tag{6}$$

It is assumed that the field lenses and Wollaston prism on the pitch side are the same as the catch side (W^{C}, FL^{1C}, FL^{2C}). The transmission through the BE, NP, and HWP^{3P} is found in Eq. (7).

$$\mathcal{T}_{\text{BE-NP-HWP}} = \frac{71.0\text{ mW}}{110.2\text{ mW}}\left(\frac{1}{0.9028}\right) = 71.36\% \tag{7}$$

Using the specifications of the BE and HWP^{3P}, the transmission for each is $\mathcal{T}_{\text{BE}} = 89.97\%$ and $\mathcal{T}_{\text{HWP}} = 99.5\%$. The transmission of the NP can be found using these values in Eq. (8).

$$\mathcal{T}_{\text{NP}} = \frac{0.7136}{(0.8997)\,(0.995)} = 79.71\% \tag{8}$$

Also from the specifications, the transmission of the LP and FO are $\mathcal{T}_{\text{LP}} = 74\%$ and $\mathcal{T}_{\text{FO}} = 91.9\%$. The reflectance of the PM is greater than 90%, and the transmission of the QWP is the same as the HWP used earlier. The agreement between the measured power and the expected transmission can be confirmed now. Note that since the beam is split by the PM, half the power before the PM is used as the incident power (64.1 mW/2 = 32 mW).

$$\frac{18.7\text{ mW}}{32\text{ mW}} = 58.4\% \tag{9}$$

$$\mathcal{R}_{\text{PM}}\mathcal{T}_{\text{QWP}}\mathcal{T}_{\text{LP}}\mathcal{T}_{\text{FO}} = (0.9)\,(0.995)\,(0.74)\,(0.919) = 60.9\% \tag{10}$$

The calculated and measured values are in good agreement, which allows predictions of laser power settings for adequate (and correct) voltages at the detectors. These measurements will be useful for future system designs to predict laser powers needed for multiple beam systems. Without anti-reflection coated optics, these losses through the system would be even larger.

III. Alignment Procedure

To ensure consistent data quality throughout the duration of the testing campaign, an alignment procedure was prescribed and adhered to when setting up and aligning the FLDI system. Alignment starts on the pitch board with the aid of a camera mounted at the test section focus. The alignment then continues on the catch board. When access to the test section is not available, the procedure in the Appendix is used.

A. Basic Component Layout

When setting up the FLDI boards for the first time, there are some items that should be taken into consideration so extensive design adjustments are not necessary later. If the system is being used for ground facility testing, consideration for the side of the board that will allow for easier physical access to optical components is important. Based on the easily accessible side, components should be placed such that their adjustment (rotation indication and locking set-screw) is simple from that side. Using a cage system for the optics along with vibration damping posts increases the rigidity, and allows for easier alignment of the laser beam along the optical axis. Where possible, lens tubes should be inserted into the cage system to confine the beam within the system and increase its safety. Rotation mounts should be extensively used because most optical components must be able to rotate with respect to each other (HWP^{1P}, HWP^{2P}, NP, HWP^{3P}, W^{P}, W^{C}, QWP^{1C}, QWP^{2C}, LP^{1C}, LP^{2C}). The indicator line on the side of the rotation mount should be visible for precise alignments, and the set screw to tighten the components in place should be accessible as well. Some optics need to be removed for alignment of the system (BE, NP, HWP^{3P}, W^{P}), so the mounts for these component should either be easily removable in full (using drop-in/quick-release cage mounts) or the optic should be able to be easily removed from the fixed mount in the cage system without moving its position along the cage system rods. These suggestions for the system setup are not fixed requirements, but are mentioned for convenience for documentation, setup, and alignment.

B. Pitch Alignment

Using the values from Table 2, the optics can be placed at roughly the correct axial locations with respect to each other (along the beam axis). A CMOS camera is then placed at the test section focus, such that the sensor coincides with the beam focus. No lenses are attached, but ND filters are used to decrease the intensity since the beam is focusing down on the camera sensor. To begin, the W^{P}, HWP^{3P}, and NP are all removed. The HWP^{1P} is used to control the power transmitted through the system, and the HWP^{2P} has no influence on this first portion of alignment, so both can remain in place. The position of the BE is first placed such that its focal point is located at the focal distance from the FL^{1P}. This is verified both by making sure the FL^{1P} is fully filled (not under- or over-filled), and by ensuring that the beam focuses down to a point in the test section at the focal length of the FL^{2P}. Once these conditions are met, the BE is locked into position, but is mounted on an axial micrometer translation stage (Thorlabs CT1) because the addition of the other optics between the BE and the FL^{1P} will necessitate slight adjustments to maintain alignment downstream.

The NP is now added to the system, with the orientation of these beams dictated by the test requirements. The NP is placed such that the convergence point of the two beams is located at the effective focal length from the FL^{P} (beams cross at the W^{P}). This distance can be verified by the camera, where the beam separation at the test section focus should be equal to its theoretical value computed in Section II.D. The BE might need to be adjusted slightly to account for the shift in test section focus due to the inclusion of the 5.08 cm long NP. The NP is rotated in its mount until the desired orientation is shown on the camera. Once the NP is aligned correctly, the HWP^{2P} is rotated such that one NP-pair beam disappears and the other is at maximum intensity (and the angle is noted). The HWP^{2P} is rotated further until the other beam disappears and the first beam is at its maximum intensity, making a note of the angle. The HWP^{2P} is set to the point of balanced (equal) intensity of the two NP-pair beams, halfway between these two angles. This gives a rough alignment of the rotation of the HWP^{2P}, but will be refined later in the alignment process using the detectors on the catch side.

The HWP^{3P} and W^{P} are now both added back in place. The HWP^{3P} can be placed anywhere between the NP and the W^{P}, limited only by the expanding beam, its clear aperture, and the ease of accessibility. The W^{P} is placed at the effective focal length of the FL^{P}, and the BE is adjusted slightly again to maintain the focus of the beams at the focal length away from the FL^{2P} in the test section. For each NP-pair beam, there should now be two W-pair beams. If these W-pairs are not visible, the HWP^{3P} is rotated until they appear. The W^{P} is rotated until the W-pair beams are in the correct orientation for the test. The HWP^{3P} is rotated as necessary with the W^{P} rotation to make sure both W-pair beams are visible as the orientation is set. The intensity of each NP-pair (sum of W-pair beams) should stay constant since the HWP^{2P} and NP are fixed. Once the orientation of the W-pair beams is set, the adjustment of the HWP^{3P} proceeds in the same way as the adjustment of the HWP^{2P}, where angles are noted for maximum/minimum intensities of opposite beams, and the balanced angle is set to the middle of the two. Every time the W^{P} is rotated, the HWP^{3P} must be rotated to balance the W-pair beams. Note that a QWP can be used instead of the HWP, such that when the QWP is properly aligned, the W^{P} can rotate freely without the need to realign the QWP (as long as the HWP^{2P} and NP orientations remain unchanged).

C. Catch Alignment

The catch board is placed in a mirrored fashion about the test section focus to the pitch board. That is, the breadboard is positioned such that the test section focus is at the focal distance away from (and the expanding beam fills) the FL^{1C}. The W^{C} is first removed from the system, and the beams are allowed to pass through to the PM, which connects L4 to L5 and L6. The components on these legs are allowed to remain in place, but the detectors ($DET^{\#C}$) are removed (where # denotes both 1 and 2 from L5 and L6). The PM-L5-L6 subsystem is rotated such that the splitting of the PM is aligned with the NP-pair orientation. The correct splitting of the two beams by the PM is easily verified by viewing the expanding beams from L5 and L6. If the PM is not oriented correctly, two beams will be visible from one leg, while none will be visible from the other (or partial beams on both). The W^{C} is then added back in place at the effective focal length away from FL^{C}, and the interference pattern is viewed from the exit of L5 and L6. The correct rotation of the W^{C} is the angle at which an infinite fringe is found, and once this is found it is locked in place. Based on the orientation of the $QWP^{\#C}$ and $LP^{\#C}$, the location on the infinite fringe will change. The polarization of each recombined NP-pair beam should be very nearly linear if no index of refraction changes exist along the beam path. The linear polarization is converted to circular polarization through the $QWP^{\#C}$, by setting the fast axis of the $QWP^{\#C}$ oriented at 45° with respect to the linear polarization axis (depends on the orientation of the NP and W^{P}). The $QWP^{\#C}$ and $LP^{\#C}$ can be rotated at the same time until a minimum intensity is found on both channels, and the $QWP^{\#C}$ are both locked in place. The $DET^{\#C}$ are now added back to the system for the final alignment. The $LP^{\#C}$ should be in approximately the best position already, but using the detectors with the smallest vertical resolution on the oscilloscope allows the signal to be minimized to the best ability of the resolution of the system.

Once the absolute minimum for both detectors is found, a data trace is acquired and the mean (minimum) voltage is noted. If the W^{C} and $QWP^{\#C}$ are aligned correctly, these voltages should be the same. The vertical resolution of the oscilloscope is increased to an appropriate level as the $LP^{\#C}$ are rotated, until a maximum signal on both channels is found. This is the brightest that can be achieved on the interference fringe. With the $LP^{\#C}$ aligned to obtain the maximum signal, the HWP^{1P} is rotated until the signal on the scope reaches the maximum linear range voltage for both channels (Section II.E). Since the $LP^{\#C}$ orientation currently positions the beam at the maximum of the interference fringe, and because the laser power will not change during the test, this ensures that the system will always operate in the linear range of the detectors. A data trace is acquired and the mean (maximum) voltage is noted. The middle of the interference fringe is located halfway between the minimum and maximum voltage signals, and the $LP^{\#C}$ are both rotated until the voltage matches the mean voltage. This results in the most linear portion of the interference fringe, and gives the best approximation of the derivative of the index of refraction field. Another data trace of both channels is acquired (mean of the middle voltage). The $LP^{\#C}$ can be adjusted if the signals have opposite but equal amplitudes such that they track with each other (one LP is rotated 180°).

D. Scope, Detector, and Fringe Linear Range and Saturation

Scope, detector, and fringe linear ranges and saturation limits are important considerations when aligning the system and acquiring signals sensitive to high frequencies, with predictable responses to density fluctuations.

Scope Saturation

The oscilloscope is set to a voltage range that ensures signal clipping will not occur. In the event the intensity incident on the detector produces a voltage that exceeds these limits, the scope will saturate, and any data outside these ranges will be clipped. It is imperative before a run to make sure the vertical resolution is set such that the scope never saturates during a test. This is difficult to determine before the first run, since the amplitude of the signal is not known beforehand. To be conservative, the maximum voltage of the detector can be set as the maximum voltage the detectors are capable of (500 mV from Section II.E). However, the signals from the FLDI system are by design much smaller than this limit, assuming the system is set to the middle of the infinite interference fringe. Depending on the bit depth of the oscilloscope, the vertical resolution of the data will be under-sampled. The best practice is to perform a nominal run at test conditions with the maximum voltage range, and narrow down the vertical resolution based on the maximum voltages recorded during the test.

Detector Linear Range and Saturation

The linear range of the detectors used in these experiments was found in Section II.E. For these photodiodes (Thorlabs DET100A2), the linear range using a 50 Ω load resistor is between 0 and 400 mV (which does not include

the non-linear region near the noise floor, since the minimum laser intensity does not reach low enough). Given the maximum voltage of the interference fringe signal is less than or equal to the maximum linear range detector voltage, then the detector will function adequately for all portions of the tests.

Interference Fringe Linear Range and Saturation

The system was initially set to the middle of the interference infinite fringe (half the amplitude of the fringe amplitude). When the phase between the two orthogonally polarized beams changes, the intensity increases or decreases by shifting the position on the fringe. The entire fringe has been spanned when the minimum and maximum signals are reached, an any increase or decrease in phase will shift the signal over to the next fringe. This creates fringe ambiguity and must be avoided. Well before the fringe saturation/ambiguity limit is reached, the voltage change due to a change in phase will deviate from being linear. As with a sine or cosine wave, the region near the origin can be approximated as linear for small enough changes in phase angle.

E. Frequency Response Attenuation

The frequency response of the photodiode depends on the fill percentage of the beam spot on the detector element for a constant power, where saturation of the photodiodes can occur at higher frequencies when a sub-optimal fill percentage is used. An example of high-frequency attenuation that occurs is shown in Fig. 8, using data under vacuum (*OnSphere*) from early runs during the testing campaign. Beam spots are generally focused such that they fill approximately 70% to 80% of the detector element's size. The three data sets on the plot correspond to low (magenta), medium (red), and high (blue) fill percentages of the beam spot on the photodiode element. The noise floor of the instrument for these measurements is approximately 10^{-16}. The optimal fill percentage (high fill) is based on the largest amplitudes of the spectral signal that were obtained during the testing campaign. When the fill percentage is low, the response of system starts to drop off from the high-fill case at approximately 1×10^4 Hz and reaches the noise floor near 1.5×10^5 Hz. With a medium fill percentage, the response starts to drop off at approximately 3×10^4 Hz and reaches the noise floor near 3.5×10^5 Hz. The high fill percentage case provides the maximum amount of sensitivity out to the highest frequencies for this specific instrument. The high-frequency response will degrade before there is any effect on the low-frequency response. Ideally, the beam spot size on the photodiode element should not change after it has been initially aligned, but every time a realignment of the system is performed, the frequency response should be tested. This can be done by introducing a high frequency disturbance (such as canned air) at the focus, taking a data set, and comparing the spectra to a known ideal frequency response case.

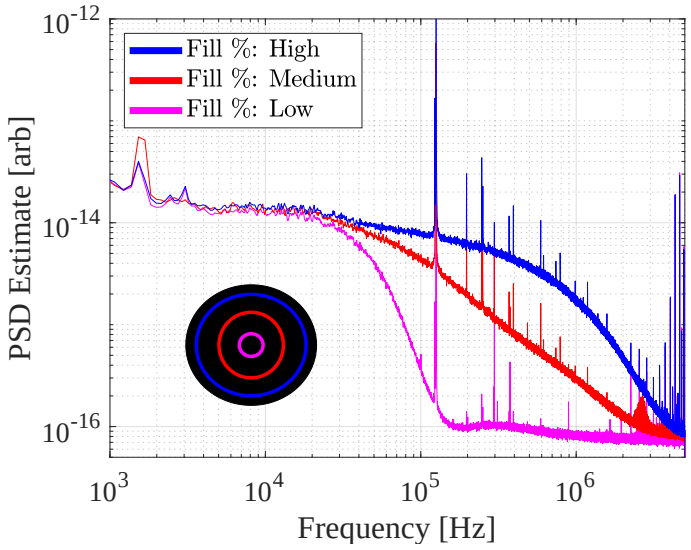

Fig. 8 Power spectral density estimate comparing frequency response attenuation with changing beam fill percentage on photodiode element. Colored circles show characteristic sizes of beams on the detector face (solid black circle).

Smaller photodiodes were used in a previous FLDI system (DET36A) [7], but a larger photodiode (DET100A2) was used here for several reasons. As light is collected near the edges of the active area of the sensor, unwanted capacitance and resistance effects can occur that distort the time-domain response of the sensor. If beam steering occurs through the flow and/or the sensor is overfilled initially, it will result in a changed spectral response. It is recommended to center the incident light on the active area and to use a focusing lens to reduce the signal near the edges. This is easier for the larger photodiode, and while rise time is decreased for larger elements (14 ns for the DET36A versus 35 ns for the DET100A2), it was still more than sufficient for these measurements.

F. Beam Location on Cone

The beam location on the cone surface is important to know accurately for comparison of FLDI and PCB results. The CMOS camera mounted on the pitch breadboard directly next to the FL^P was used to determine the beam spot locations on the model. A schematic of the PCB sensors and FLDI beam location on the cone for Runs 82 - 93 can be seen in Fig. 9a. The two flush-mounted PCB sensors closest to the FLDI beam spots are located on the 90° ray (top of the cone), at 292 mm (PCB19) and 343 mm (PCB20) back from the tip of the cone. The cone comprises a nose tip, the S1 base (which the nose tip attaches to), and the S2 base (which the S1 base attaches to). The S1-S2 base seam is located 279 mm from the nose tip. The upstream PCB (green), upstream FLDI (blue), downstream FLDI (red), and downstream PCB (magenta) are all color-coded to match results later in this paper.

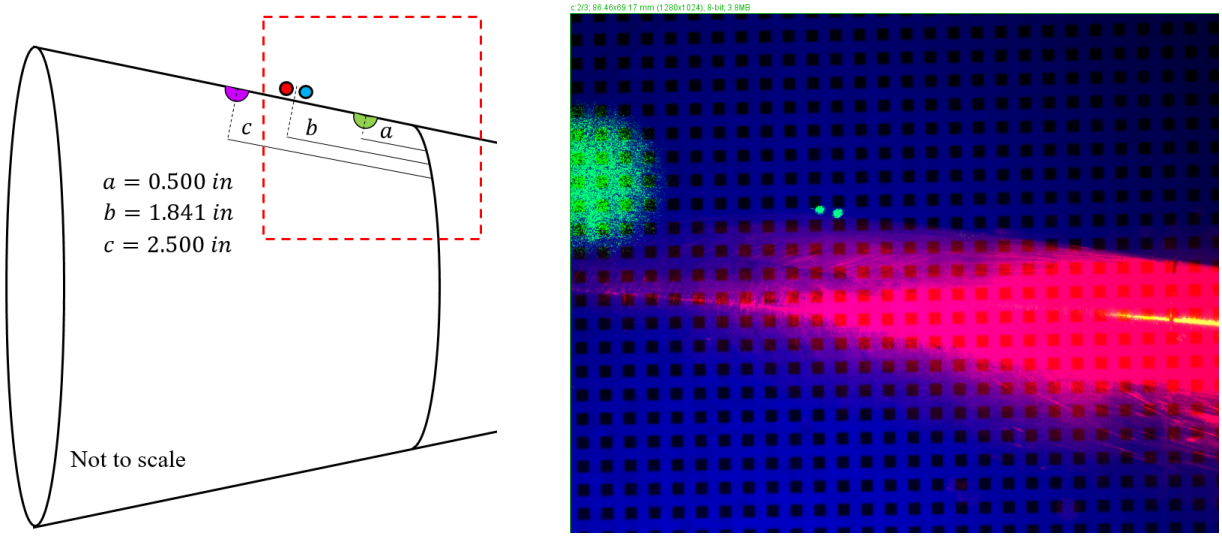

(a) **(b)**

Fig. 9 (a) Schematic of cone and sensor locations with red dashed FoV for (b) composite image for beam spot location verification including (green) laser spots, (red) S1-S2 base seam, and (blue) dot card.

The calibration images from the CMOS camera can be seen in Fig. 9b, where the dashed red box in Fig. 9a indicates the field of view. With a dot spacing of 3.175 mm, the scale for the calibration is 14.4916 pixels/mm. The distance from the S1-S2 base seam (seen near the right edge) to the center of the NP-pair is approximately 46.77 mm (1.84 in). Thus, the center of the NP-pair is located at 326 mm, between PCB19 and PCB20. The NP-pair separation from this image is 2.497 mm, which is very nearly the calculated value of 2.473 mm from the NP divergence angle (Section II.D).

When the model is injected and reaches its centerline position, there is a period of oscillation of the cantilevered model before it dampens (this depends on the injection setup). A high-speed schlieren video was used to determine how the cone edge moves with time, resulting in a cone oscillation frequency of approximately 60 Hz. When an NP-pair beam is aligned exactly to the cone edge, this oscillation early in time can also be seen as the signal cuts in and out early in the run (Fig. 10). The beginning of the two second FLDI acquisition is delayed by 2 seconds from the initial trigger to avoid the oscillations of the model after it has just been injected, but cutout still occurs for a short period after. The drop-out of FLDI signal was repeatable from run-to run. When the drop-out of signal was not seen in the FLDI, it could be deduced that the beam spots were farther off the surface of the cone.

The data shown in Fig. 10 is from Run 22, using configuration B from Fig. 5b. From the zoom inset in Fig. 10, it is

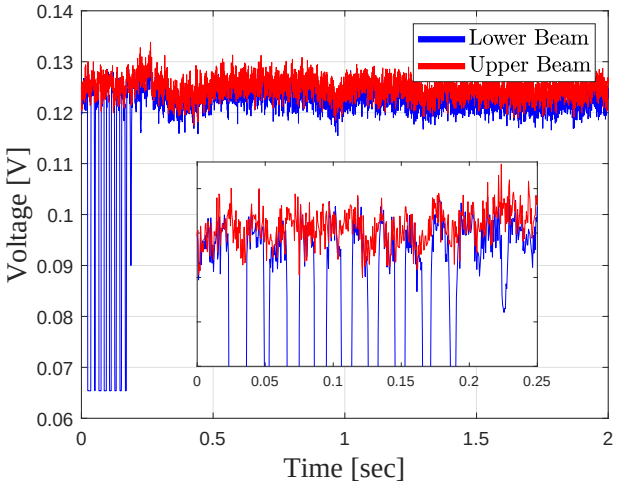

Fig. 10 Cutout of lower NP-pair beam signal early in time for Run 22 (configuration B). Every 5000^{th} sample shown for clarity.

more easily seen that the lower beam cuts out but the upper beam does not. This shows that upon injection, the cone oscillates (at approximately 60 Hz) about its final resting position, but does not oscillate with such a magnitude that it blocks the top beam as well.

IV. Spark Test Results

To assess the response of the FLDI system, one method that has been used successfully is the spark test, where a highly-repeatable acoustic wave is generated and the response of the FLDI signal is characterized [30]. Nine spark test cases with various beam orientations were were performed, shown in Fig. 3a (wave traveling from top to bottom of the frame), and each labeled with a corresponding letter, (a) through (g). The wave was generated from LIB above the plane of the FLDI and HSS systems (Fig. 2).

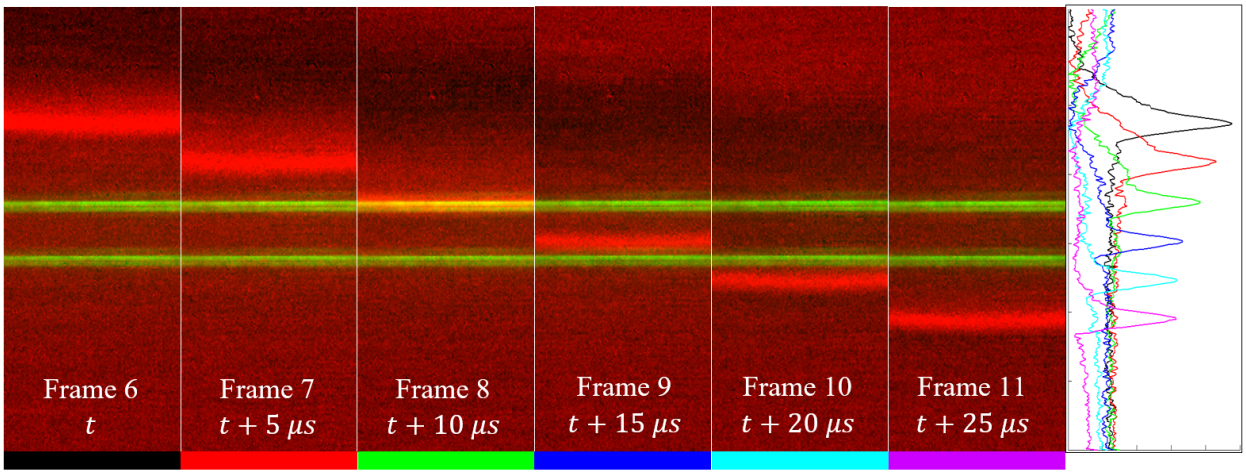

Fig. 11 Primary train of LIB-generated wave with background-subtracted schlieren data (red) and overlay of FLDI beam profile (green). Plot on the far right shows instantaneous schlieren wave intensity profile for the appropriate frame.

The FLDI beam profiles at the test section focus, taken with a CMOS camera (Fig. 3b), provide a clear visual of the exact orientation and separation of the W-pairs and NP-pairs for each case. The vertical separation distances

between the NP-pairs are (a) 2.432 mm, (b) 2.434 mm, (c) 2.432 mm, (b-f) 0 mm, (g) 1.763 mm, (h) 1.761 mm, and (i) 1.766 mm. The vertical separation between the W-pairs for the cases shown are (a) 255.3 μm, (b) 193.2 μm, (c) 0 μm, (d) 255.3 μm, (e) 186.3 μm, (f) 0 μm, (g) 255.3 μm, (h) 179.4 μm, and (i) 0 μm. These separation distances were found by fitting Gaussian profiles to the beam spots to obtain sub-pixel accuracy of the peak separation distances. Note that the measured W-pair beam separations (255 μm) are slightly different than the theoretical separation from Eq. (2) (218 μm), but is also on the order of the same difference seen between the measured and theoretical NP-pair beam separations (2.43 mm and 2.47 mm).

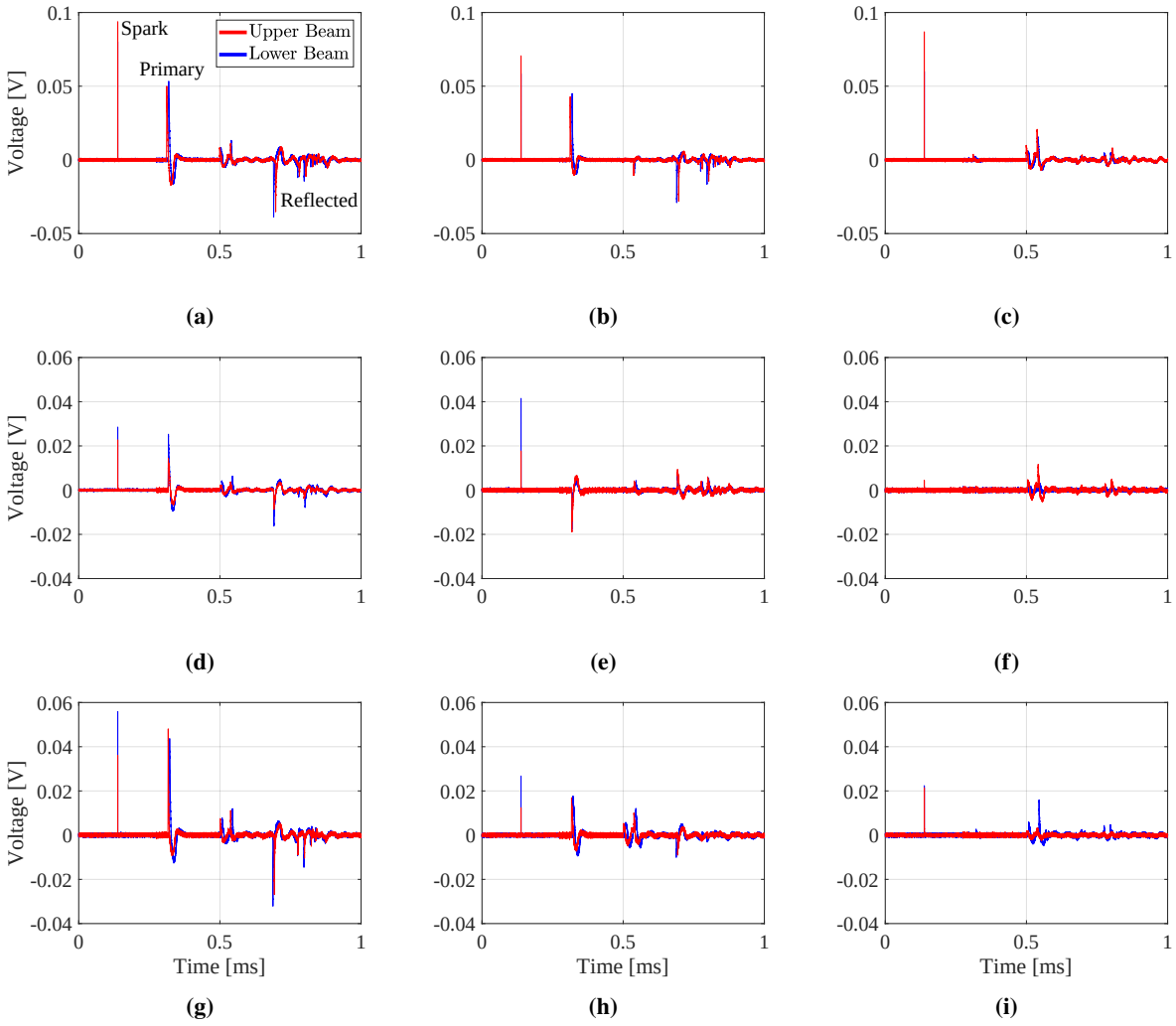

Fig. 12 FLDI time traces for cases (a-i), with colors corresponding to the beam positions based on Fig. 3.

The frame rate and calibrated length scale of the HSS system (subscript S) was first used to compute the velocity of the wave for both primary and reflected waves (V_S^P and V_S^R, respectively). Case (a) is used to demonstrate some results, and then results from the other cases are summarized. For case (a), the LIB wave travels from the top of the frame downwards, first passing through the top NP-pair beam (first the top W-pair beam, then the bottom W-pair beam) and then through the bottom NP-pair beam. At a large enough distance from the spark, the spherical wave from the spark can be considered a plane wave, and since the W-pairs are oriented vertically, the two beams will experience differences in their polarization state with time as the shock progresses downwards. The change in polarization of each beam results in a change in phase, and a signal increase or decrease on the oscilloscope depending on whether the index of refraction increased or decreased, and on which W-pair beam was affected first.

In Fig. 11, six successive frames of the HSS with overlaid FLDI beam profiles for case (a) can be seen. The beam profiles were acquired by spraying canned air through the FLDI beam focus, and averaging 200 images together.

Although faint, the W-pair can be seen in each NP-pair beam. An average of the vertical profile over the horizontal width of the HSS image was extracted for each frame, and the peak intensity of the resulting profile was found for each (right edge of Fig. 11). Using the spatial calibration of the schlieren FoV, the pixel difference was converted to a physical distance, and then divided by the time between frames to obtain the velocity. The mean velocity over the four frames where the wave passed through the FLDI beams was used as the final wave velocity from the schlieren measurements. The velocity of the reflected wave was computed in the same way that the primary wave velocity was computed. Based on the precisely measured distances from the NP-pairs to the aluminum plate and the time delay between the primary and reflected signals of the FLDI, the velocity could again be verified.

The 1-second FLDI time trace for each case are shown in Fig. 12. For cases (d) through (f) that do not have a top/bottom beam, the top beam label corresponds to the left beam and the bottom beam label to the right beam (in Fig. 3). The narrow spike seen in every data set at 0.1383 sec is the LIB laser firing. Note that the vertical scales are the same for cases (a) through (c) and (d) through (i), but different between those two groups. Plots for case (a), (d), and (g) all have the W-pairs aligned vertically, and exhibit the largest signal fluctuations as the wave passes through them. Plots for case (b), (e), and (h) have the W-pairs aligned at 45°, and thus see a reduced signal. When the W-pairs are aligned horizontally as they are for cases (c), (f), and (i), no signal (or extremely little due to the system's high sensitivity) is seen for the primary and reflected waves, because the disturbance passes through both W-pair beams at the same time, inducing the same phase shift on each beam, which when recombined does not change the intensity on the detector. These small signals encountered when none should be present demonstrates the sensitivity of the system. Between the primary and reflected waves, there is signal that looks like a weaker wave. This signal is from the primary wave reflecting off the schlieren lens and mount, which reflects back into the beam path before the reflected wave reaches the FoV again. The wave from the lens, which is located to the left of the frame (when looking at the CMOS beam profiles in Fig. 2b), reflects back at an oblique angle (from the top-left of the frame to the bottom-right). The signal from this reflected wave should then always register first on the upper/left beam (red), which is indeed what happens for every case. This signal also registers for the cases that are insensitive to the primary/reflected wave due to horizontal W-pair orientation (cases (c), (f), and (i)), because the angle of the lens-wave passes through the W-pairs at a different angle. An example of the 180° out of phase rotation of the $LP^{\#C}$ is shown in case (e), where the primary wave registers as an initial decrease in signal, and the reflected wave as an increase in signal. The interpretation of the results is the same as the other cases, only with the signals inverted. When frequency information is intended to be gathered from the data, this 180° phase shift is inconsequential. However, if velocity information is desired from the cross correlation of the time signal, then at minimum it should be ensured that both signals have the same $LP^{\#C}$ orientation.

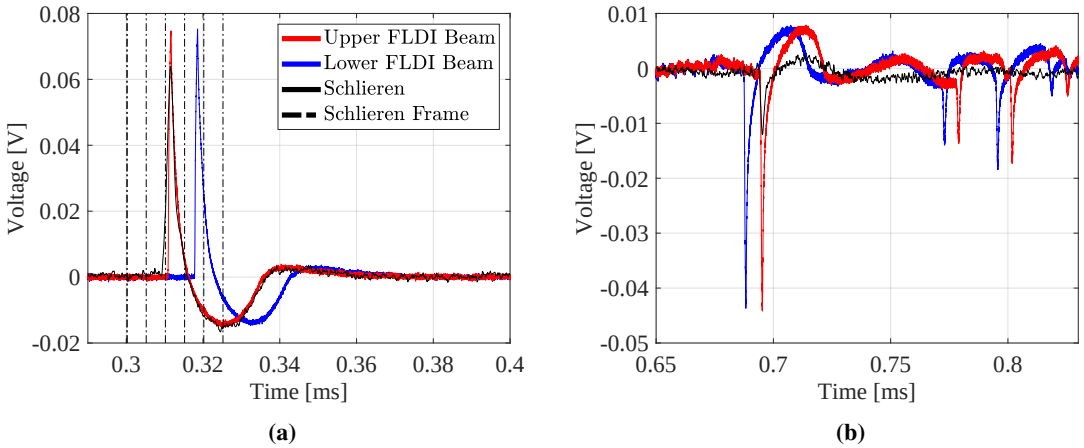

Fig. 13 Zoomed view of the (a) primary and (b) reflected wave signal for the two FLDI NP-pair beams (red, blue) and the reconstructed schlieren data (solid black). The six HSS frames shown in Fig. 11 are denoted by the black dash-dot line.

The schlieren raw data is a set of frames (where six of these frames are shown in Fig. 11), each with the wave progressing farther down in the FoV as time increases. This wave is nominally the same shape (ignoring viscous diffusion in the 20 μs acquisition window) for the time that it takes it to pass down and reflect back up through the FoV. By finding the pixel shift of the wave peak for each frame, the vertical profile of the wave from each frame is

Table 3 Spark test HSS and FLDI results for each case with 95% confidence intervals.

Case	V_S^P, m/s	V_S^R, m/s	V_{FLDI}^P, m/s	V_{FLDI}^R, m/s
(a)	348.91 ± 2.48	342.78 ± 7.38	349.45 ± 0.8	345.09 ± 1.9
(b)	348.99 ± 1.59	344.00 ± 8.22	351.16 ± 0.5	347.15 ± 0.5
(c)	347.58 ± 1.63	343.98 ± 3.55	-	-
(d)	346.43 ± 2.08	344.19 ± 4.31	-	-
(e)	346.55 ± 2.23	341.43 ± 5.38	-	-
(f)	347.17 ± 2.42	343.64 ± 4.03	-	-
(g)	345.83 ± 2.69	344.92 ± 7.34	344.76 ± 2.7	339.41 ± 2.6
(h)	347.18 ± 1.72	345.90 ± 3.87	345.98 ± 3.0	332.76 ± 1.4
(i)	346.84 ± 1.93	342.79 ± 9.30	-	-

shifted relative to the next frames by the pixel shift of the peak, and all the profiles from the 200 frames are averaged together. This gives a reconstructed view of the wave as an intensity as a function of time, which can be compared to a voltage trace of the FLDI data in Fig. 13. Since the schlieren data (solid black) is reconstructed in time, it is arbitrarily aligned with the upper FLDI beam data (red). The schlieren signal is also scaled vertically to match the FLDI signal for comparison since the FLDI is measured as a voltage and the schlieren as a pixel intensity. The vertical dashed black lines indicate the frames of the HSS acquisition, corresponding to the same six frames from Fig. 11.

The primary wave (Fig. 13a) begins with an upwards spike, corresponding to an increase in density, and is followed by a quick decrease in voltage to negative values corresponding to the following expansion. This can also be seen in Fig. 11 where the bright red is the increase in density and the darker (tending towards black) portion is the expansion region. There is also a slight overshoot in signal as it levels off again. All three of these characteristics (peak, dip, overshoot) are captured by both the FLDI and schlieren systems. The reflected wave (Fig.13b) begins with a downward spike, this also corresponding to an increase in density, but because the bottom W-pair beam is being traversed first, the voltage level is inverted. The bottom beam sees the reflected wave first as is expected, and a short time later the top beam sees the same wave. The vertical profiles of the two NP-pair beams are nearly identical, indicating equal balancing of the signals. The reconstructed schlieren signal again coincides with the top FLDI signal, and again sees the same peak and dip from the primary wave results (although inverted now). Because the signal is weaker for the reflected wave, there is no visible overshoot in the schlieren data, although there might be some visible in the FLDI data which is more sensitive. Also of note is that the schlieren intensity signal (which has been normalized to the FLDI top beam data) is significantly lower in amplitude for the reflected wave than the FLDI.

The schlieren velocity results along with a 95% confidence interval can be seen in Table 3 for both primary and reflected waves. The FLDI velocities can be computed from only four cases ((a), (b), (g), and (h)) because the other cases have either NP-pairs horizontal, W-pairs horizontal, or both, which result in signals either overlapping in time (no offset) or no signal at all. Agreement between FLDI and schlieren velocities verifies the use of the FLDI system to compute velocities of ground test facility density disturbances.

V. 20 Inch Mach 6 Results

A. Run Summary

Testing was conducted at the 20-Inch Mach 6 air tunnel with a total of 93 runs conducted, with only one run (Run 9) discarded due to the model failing to inject properly. Run characteristics including the FLDI configuration, nose tip radius, and unit Reynolds number are shown in Table 4. The four configurations in this table are shown in Fig. 5. The unit Reynolds numbers listed in the table are approximate, as there can be deviations of $\approx 0.08 \times 10^6$ ft^{-1} for specific runs about their listed mean value. Pre-run data under vacuum (*OnSphere*), model-injected data (*ModelInjected*), and post-model-retraction freestream data (*Freestream*) were acquired for each run.

Runs 82 through 93 were taken with the beams farther back on the cone (configuration D in Fig. 5), and visible peaks in the power spectral density (PSD) from second-mode waves were clearly seen. Data from these runs is shown in Fig. 14, which for this plot includes just the upstream FLDI data, although downstream data is nearly identical. The

Table 4 Configuration, nose tip radius, and unit Reynolds number for all 20-Inch Mach 6 runs.

Characteristic	Runs	Re ($\times 10^6$ ft^{-1})	Runs
Config. A (Fig 5a)	1-5	Re = 1.0	36
Config. B (Fig 5b)	6-68	Re = 1.5	19, 37
Config. C (Fig 5c)	69-81	Re = 2.0	38
Config. D (Fig 5d)	82-93	Re = 2.5	18, 34
R_n = 0.006 in	31-39	Re = 3.0	17, 33, 89
R_n = 0.080 in	2-20, 77-93	Re = 3.5	16
R_n = 0.110 in	21-30	Re = 4.0	2-5, 13, 21, 31-32, 43, 88
R_n = 0.150 in	40-45	Re = 4.5	12, 23
R_n = 0.175 in	46-49	Re = 5.0	11, 22, 35, 69, 86
R_n = 0.200 in	50-54	Re = 5.5	10, 24, 90, 92
R_n = 0.250 in	55-60	Re = 6.0	8, 25, 40, 50, 61, 85
R_n = 0.300 in	72-76	Re = 6.5	26, 91
R_n = 0.375 in	70-71	Re = 7.0	7, 27, 41, 46, 51, 55, 68, 71, 73-74, 77, 81, 84
R_n = 0.500 in	61-69	Re = 7.5	1, 28, 42, 47, 54, 56, 58, 78, 93
-	-	Re = 8.0	14-15, 20, 30, 44, 48, 52, 57, 59, 62, 64, 79, 83
-	-	Re > 8.0	6, 29, 39, 45, 49, 53, 60, 63, 65-67, 70, 72, 75-76, 80, 82, 87

Welch analysis used a window size of 2^{16}, and an overlap percentage of 50% for the Hanning window, resulting in a frequency resolution of 152.6 Hz since the data was sampled at 10 MHz. The drop off of in the signal as the frequency decreases below $\approx 2 \times 10^4$ Hz may be due to the reduced response with increasing wavelength (and thus decreasing frequency). A response coefficient for the drop off at decreasing frequencies can be computed [20], but was not applied to data in this study. For all the foregoing PSD estimates, it should be noted that no system transfer functions have been applied. The peak frequencies of the second-mode disturbance at the various Reynolds numbers were located by fitting the region near the second-mode peak ($\approx$ 330 kHz) with a low order polynomial and finding its peak, which are then plotted in Fig. 15 on the left axis. As the Reynolds number increases, the boundary layer thickness decreases, resulting in an increase of the second-mode acoustic wave frequency that can be seen in Fig. 15. The maximum PSD value at the second-mode peak is plotted on the right axis (normalized to the maximum peak value) along with an exponential fit in unit Reynolds number.

B. Freestream Repeatability

The freestream frequency content for all runs with the same unit Reynolds number should remain constant. To demonstrate the repeatability of the instrument, multiple runs for $Re = 7.5 \times 10^6$ ft^{-1} are plotted in Fig. 16a. Data from several of these runs were acquired using different W-pair and NP-pair orientations, however the general spectral trends across all configurations remains relatively constant. A similar plot for $Re = 8.0 \times 10^6$ ft^{-1} is shown in Fig. 16b. Data from only one NP-pair beam is shown, but the results from the second are the same.

At lower frequencies below $\approx 10^5$ Hz, the freestream content is nearly identical. Above 10^5 Hz, the spectra are very similar, but do have differences from run-to-run not seen at lower frequencies. Also of note is that the vertical axis is on a log scale, so differences at higher values will appear attenuated. To understand the differences in the spectra between 10^5 and 10^6 Hz, a spectrum from Run 68 can be examined ($Re = 7.0 \times 10^6$ ft^{-1}). In this run, a trip was included on the cone upstream of the FLDI measurement location such that fully turbulent flow was induced. The resulting spectra for *OnSphere*, *ModelInjected*, and *Freestream* data are shown in Fig. 17. The flow is turbulent for the *ModelInjected* data, but below 10^5 Hz, the spectra for it and the *Freestream* data are the same. At frequencies higher than 10^5 Hz, the influence is primarily due to turbulence (this is also seen to be the case in the second-mode data shown later). This indicates that the smaller scale fluctuations between 10^5 and 10^6 Hz in the freestream data from run to run are turbulent fluctuation differences in the tunnel freestream/tunnel wall boundary layer. Roll-off trends are also shown for the *ModelInjected* and *Freestream* data before 1×10^5 Hz ($f^{-13/3}$), the *Freestream* data between 1×10^5 Hz and

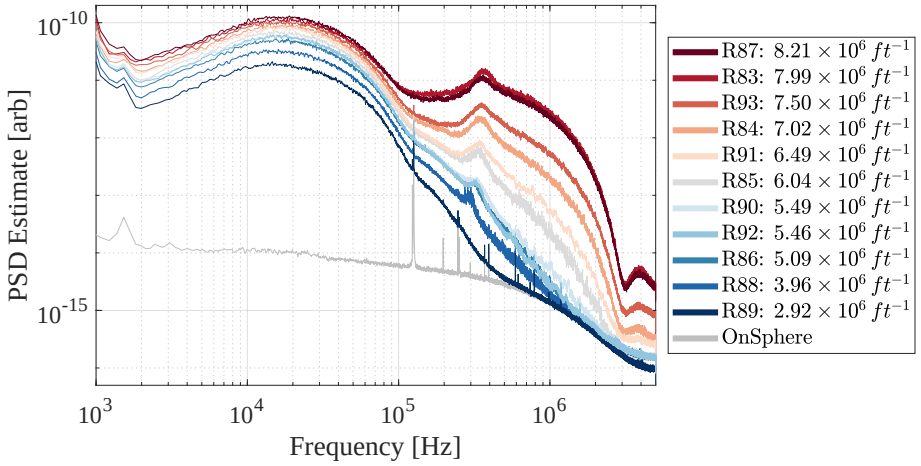

Fig. 14 Power spectral density estimates for runs in configuration D (see Fig. 5).

.

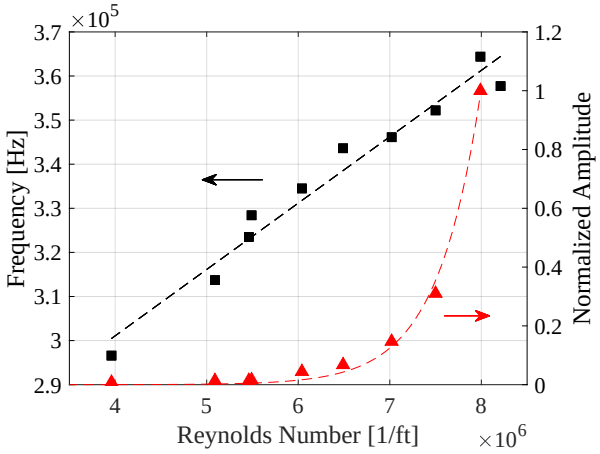

Fig. 15 Frequency (left) and amplitude (right) of second-mode peaks as a function of unit Reynolds number from full time series data sets.

5×10^5 Hz ($f^{-10/3}$), and the *ModelInjected* data between 1×10^5 Hz and 1×10^6 Hz ($f^{-5/3}$). The *Freestream* data roll-off trends are the same for all Reynolds numbers, even though the magnitude of the PSD spectra increases with increasing Reynolds number.

In both freestream plots of Fig. 16, a distinct peak in spectral content is visible near 1.8 MHz. The frequency at which this peak is located does not change for different Reynolds numbers, but the amplitude of the peak increases with increasing Reynolds number. Similarly, a peak is visible near 3.4 MHz in Fig. 14, and has the same characteristics as the 1.8 MHz peak. The origin of these peaks is unknown at this time, and further investigation is needed.

C. Flow Features

The PSD calculated using Welch's method provides a convenient view of the frequency content in a recorded signal, but does not include information about how the frequency content varies in time. To see how frequency content changes in time, a spectrogram is typically used [19–22, 27]. The spectrogram plots the frequency on the Y-axis, the time on the X-axis, and the amplitude of the frequency content on the Z-axis (darker shades indicate larger values). From the spectra for the second-mode runs in Fig. 14, a peak at the second-mode frequency is visible along with some broader signal above 10^5 Hz, although it is unclear what part of the time series this frequency content belongs to, since Welch's method essentially averages many small time window spectra together.

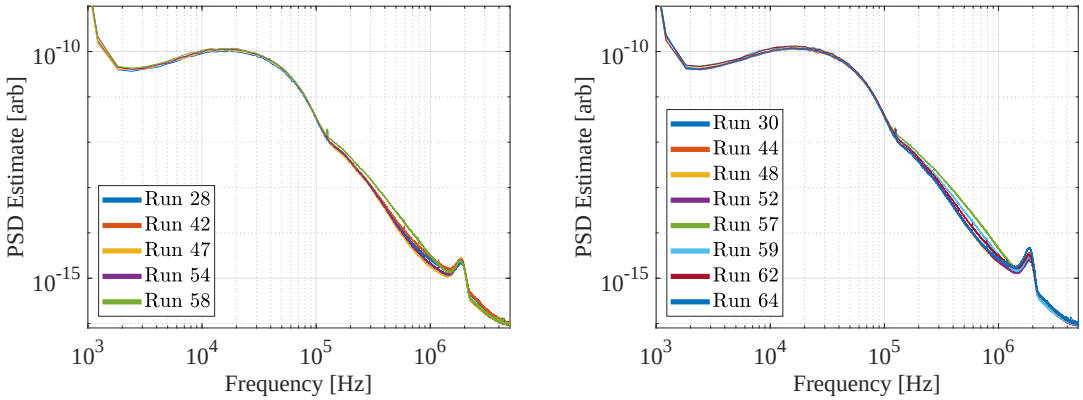

Fig. 16 Freestream spectral data (upstream NP-pair beam only) for all runs at (a) $Re = 7.5 \times 10^6$ ft^{-1} and (b) $Re = 8.0 \times 10^6$ ft^{-1}. Data from downstream NP-pair beam is nearly identical.

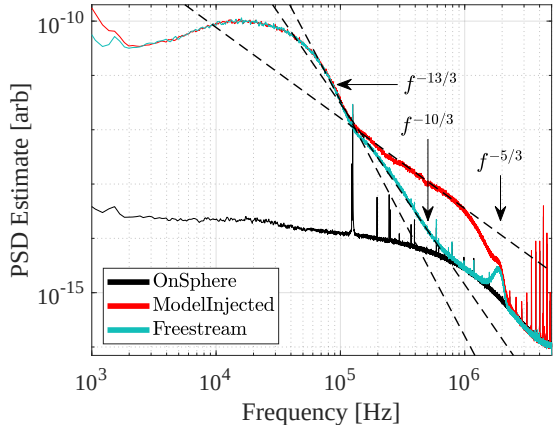

Fig. 17 Run 68 turbulent trip upstream of FLDI measurement location. Three data sets (upstream NP-pair beam only) acquired during Run 68 are shown.

The spectrogram for the upstream NP-pair beam in Runs 87 and 91 is shown in Fig. 18, which is used to identify four distinct flow features: background flow fluctuations, second-mode packets, second-mode plus harmonics (hereafter simply called harmonics), and turbulent spots. No filtering has been performed on the raw data shown in the time series plots. In Fig. 18a, the majority of the signal is broadband, low-amplitude background fluctuations. At 1.1834 sec, a distinct second-mode packet is visible as an isolated peak in both time and frequency. The plot above the spectrogram shows the corresponding time series, indicating that a second-mode packet is hard to visually differentiate from the background fluctuations. In Fig. 18b, two more flow types can be seen. Near 0.6545 sec, two harmonic packets are visible, the later one a little clearer than the earlier one. These are characterized by multiple well-defined peaks in frequency space. The last flow type, turbulent spots, are visible by the broadband signals that span the entire frequency space at discrete times, such as the one directly following the second harmonic packet. Unlike the second-mode packet, the harmonic packet and turbulent spot time-series data can be visibly differentiated from the background noise, as evidenced by the time series plot above the spectrogram.

The corresponding spectra are shown in Fig. 18c for Fig. 18a, and in Fig. 18d for Fig. 18b. The full time series spectrum (2 seconds of acquisition) of the *ModelInjected* data is shown in gray for reference. In Fig. 18c, the *Freestream* full time series spectrum is also shown in gray. Recall that plots (a) and (c) use data from Run 91 while (b) and (d) use data from Run 87, which is why their full time series spectra are different. The background fluctuation in Fig. 18c falls on the *Freestream* spectrum, and shows no narrow band peaks. The second-mode spectrum on the other hand,

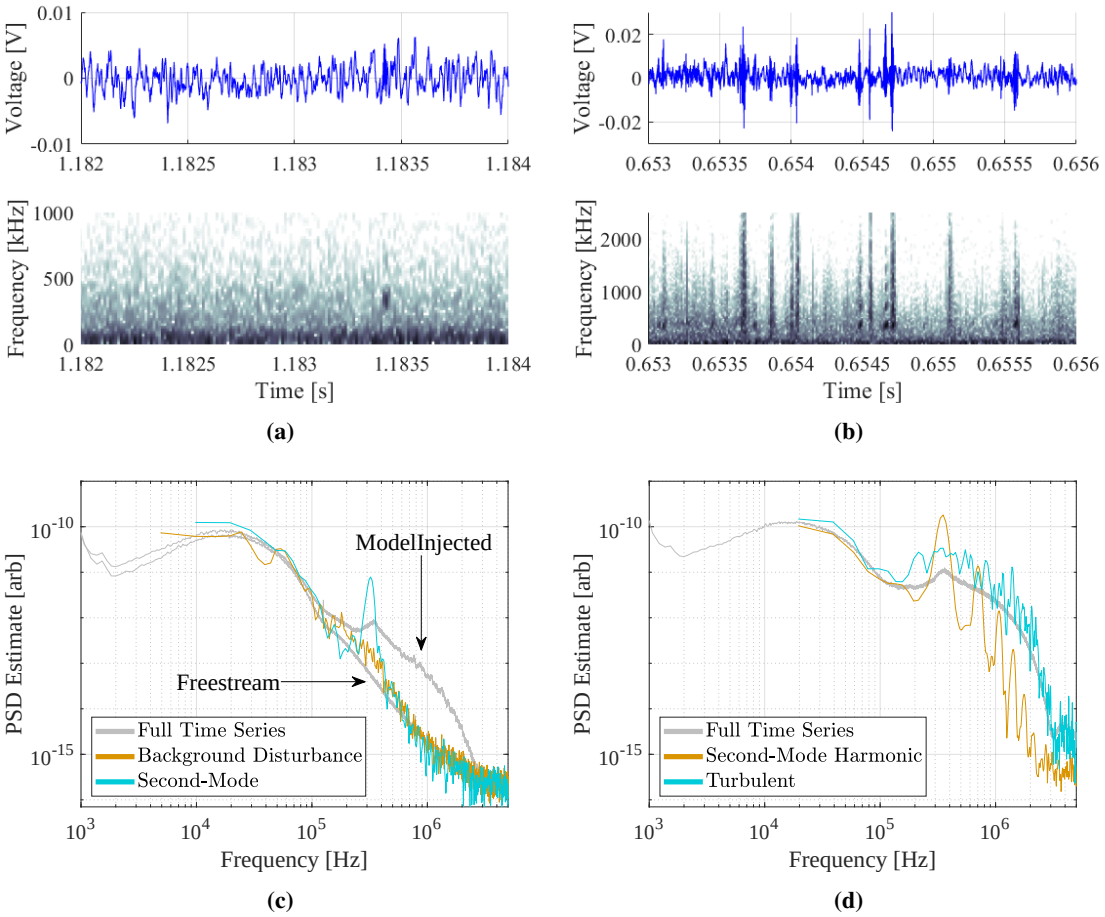

Fig. 18 Spectrogram data showing four flow types, including (a) background fluctuations and second-mode packet (Run 91), and (b) second-mode plus harmonic packet and turbulent spots (Run 87). Corresponding spectra are shown in (c) and (d) for data in (a) and (b), respectively.

shows a distinct narrow-band peak near 330 kHz, which is much narrower than the peak seen in the full time series spectrum because that peak is averaged together with the high-amplitude turbulence signals at the nearby frequencies. A better estimate for the actual second-mode frequency can then be found from each second-mode packet itself, not the full spectrum as was done for Fig. 15. The harmonic packet in Fig. 18d shows the clearly defined peaks at harmonic frequencies of the main second-mode peak. This particular harmonic packet has six distinguishable peaks, but other harmonic packets have been observed to have anywhere from two to six. The turbulent spot spectrum indicates the origin of the broadband nature of the full time-series spectrum, as it has high-amplitude frequency content from 10^5 Hz all the way out to the spectrum's edge, including the increase in signal near 3.4 MHz.

There are a number of ways to automate the process of finding second-mode packets in a time series [31]. Turbulent spots and harmonic packets can be generally identified using the unfiltered time series data since the amplitude of the voltage rises well above the background noise level (Fig. 18b), although the two can not be distinguished from each other using only this information. Second-mode packets generally do not have a voltage level above that of the background fluctuations (Fig. 18a), which makes a voltage threshold-based identification strategy ineffective. The different flow types each have a distinct signature in frequency space though, so a simple peak-integral ratio method is used here. For every point in time, three data sets are extracted from the spectrogram. The first is centered at the second-mode peak frequency ($f_{2\text{nd}} \approx 330$ kHz), and is the integral of the amplitude (Z-axis of the spectrogram) $\pm df$ about the center frequency. The second data set is found similarly by taking the amplitude integral for a frequency range lower than the second-mode peak ($f_{\text{low}} = f_{2\text{nd}} - 1e5$ Hz $\pm\, df$). The third data set is found by taking the amplitude integral for a frequency range higher than the second-mode peak ($f_{\text{high}} = f_{2\text{nd}} + 1e5$ Hz $\pm\, df$). A lower threshold is set

that defines the value above which the signal is considered a valid peak, and then the peaks in each of the three data sets are identified. If a certain location in time has a peak in each of the three data sets, it is considered to be a turbulent spot. If it has a peak in the second-mode data set, but not in the other two, it is considered a second-mode peak. The same can be extended for harmonic peak detection. A validation step is added after the automatic second-mode packet and turbulent spot identification process, which uses the PSD spectrum of the identified region for verification. In every Reynolds number case, the number of correctly identified second-mode packets ranged from 88% to 97%. The method was deemed sufficient since the incorrectly identified packets could be quickly and easily discarded in the validation step. From this method, the number of second-mode packets and turbulent spots was identified for each run, where the number of packets/spots per unit time (packet/spot rate) is plotted in Fig. 19a. As Reynolds number increases, the number of second-mode packets increases up to $Re = 6.5 \times 10^6$ ft^{-1}, and then begins to decrease again as more of these packets have transitioned over to turbulent spots. This can be seen in the turbulent spot data, where there is a increase in spots with increasing Reynolds number, but when the number of second-mode packets starts to decrease, the slope of the turbulent spot rate increases slightly (black dashed lines).

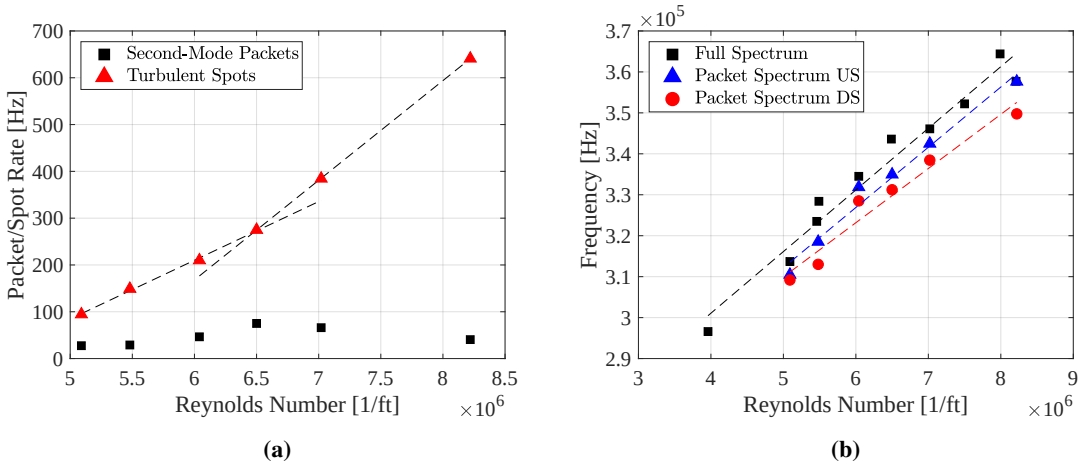

Fig. 19 Plots for (a) second-mode packets and turbulent spots per unit time as a function of unit Reynolds number and (b) second-mode packet peak frequency from full 2-second time series (black squares, upstream), identified upstream packets (blue triangles), and identified downstream packets (red circles).

As mentioned in Section V.C, a more accurate way of finding second-mode peak frequencies is to use each second-mode packet spectrum, not the full time series spectrum as was done in Section V.A. After all the packets were identified, the peak frequencies of each packet were recorded and averaged over all second-mode packets for each Reynolds number run. In Fig. 19b, the data from Fig. 15 is plotted with black squares. The packet-specific peak frequencies are plotted for both upstream (blue triangles) and downstream (red circles) FLDI data. The slope using the packet-specific technique is very similar to the full time series spectrum, but is shifted to lower frequencies, which can be seen in Fig. 18c. The higher peak frequencies from the full spectrum are due to the artificial shifting of the peak due to the broadband turbulence. The downstream peaks are also seen to have a lower frequency in accordance with the boundary layer increasing in size and decreasing the frequency of the acoustic wave.

D. Second-Mode Packet Speed and Duration

Up to this point, all the data processing has used unfiltered time series (no pre-processing of the raw data). With the second-mode peak frequencies identified for each Reynolds number, a narrow bandpass filter is used to isolate a range of frequencies near the peak. For a specified time range about the packet center-time, the envelope of the wavepacket is found. By specifying a threshold percentage of the peak voltage to background noise voltage of the envelope, the time bounds of the packet are identified. The threshold used in this paper is 20% of the peak height, but this is arbitrary and is only used to compare trends. In Fig. 20a, the filtered time series data ($\pm 5 \times 10^4$ Hz about the peak frequency) is plotted for both channels, along with the envelope and packet time bounds. The packet width is the duration between the two time bounds. Other papers have reported packet and spot duration, but it may be difficult to accurately compare because this method of determining packet width is different than others. For Run 91, the packet duration for every

identified second-mode packet in the 2-second run time is shown in Fig. 20b. The upstream and downstream data have on average the same packet duration.

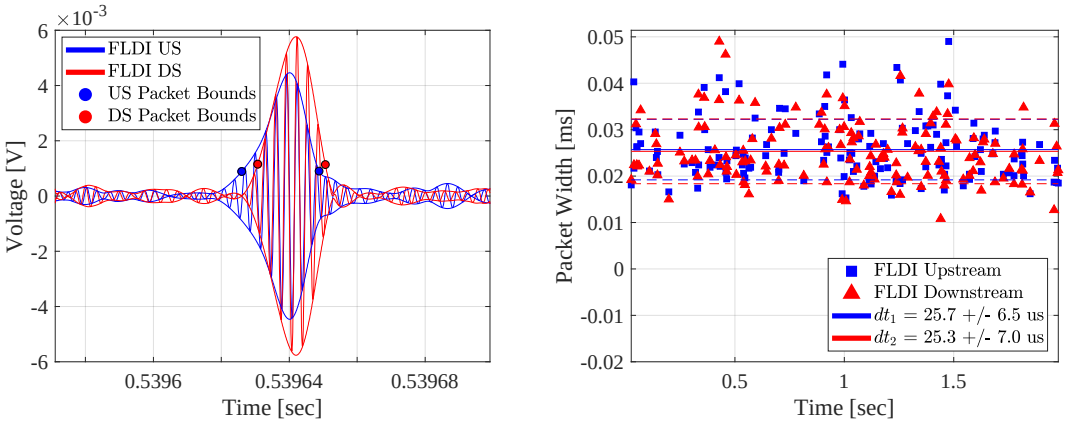

(a) **(b)**

Fig. 20 Plots for (a) the filtered packets with envelope and time bounds, and (b) the packet time duration/width. Dashed lines indicate standard deviation bounds.

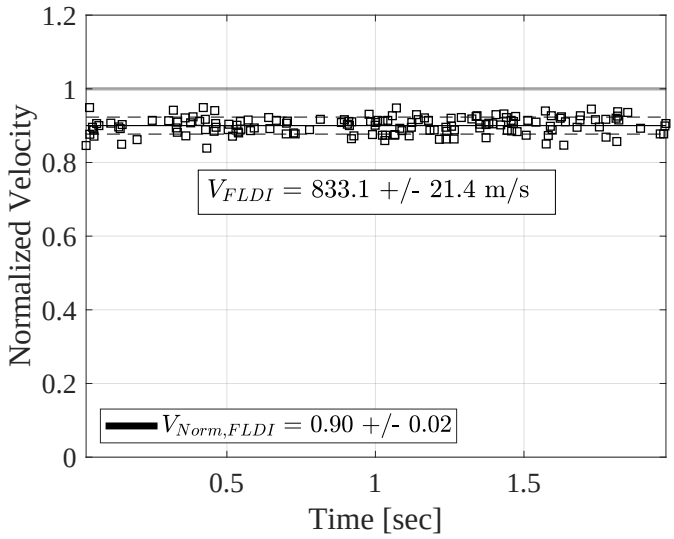

Fig. 21 Second-mode packet normalized velocities over 2-second run time for Run 91.

The two FLDI NP-pair beams are separated by a small distance (2.47 mm), so the convective velocity of the second-mode packet can be found using a cross correlation between the two filtered data sets. The time lag is converted to a velocity by dividing the NP-pair spacing by the time lag between the two signals. The velocity is further normalized by the computed freestream velocity based on inputs from the tunnel data acquisition system [32], which for the 20 Inch Mach 6 tunnel is generally near 920 m/s; a normalized velocity of unity means the packet was traveling at the freestream velocity. A plot of the normalized velocities for each second-mode packet of Run 91 is shown in Fig. 21, along with the mean velocity and normalized velocity indicated. Results for all runs can be seen in Table 5. As the Reynolds number increases, the normalized velocity decreases slightly, but the standard deviation remains generally the same.

While the most obvious application of the two-point system is for the velocity calculations for the discrete second-mode packets, the same cross correlation method can be used for the freestream data, without the model injected in the tunnel. From these measurements, the mean freestream velocities from the FLDI system are typically equal to

Table 5 FLDI second-mode packet velocities and facility freestream-normalized velocities.

Run	Re ($\times 10^6$ ft^{-1})	V_{FS} (m/s)	V_{FLDI} (m/s)	Normalized V_{FLDI}
86	5.09	923.7	849.5 ± 30.8	0.92 ± 0.03
90	5.48	924.2	837.0 ± 21.9	0.91 ± 0.02
85	6.04	923.4	837.8 ± 26.4	0.91 ± 0.03
91	6.50	925.5	833.1 ± 21.4	0.90 ± 0.02
84	7.02	924.8	830.7 ± 25.5	0.90 ± 0.03
87	8.22	924.1	814.3 ± 20.3	0.88 ± 0.02

approximately 90% of the tunnel freestream velocity. From experiments and simulations, there is general acceptance that the freestream disturbances travel down the tunnel core at approximately 60% to 70% of the freestream velocity of the tunnel. The results obtained from the cross correlation of the two-point FLDI freestream data points to a much higher velocity. This, however, may be due to sensitivity of the system away from the FLDI focus to the tunnel wall turbulent boundary layer. As shown in Deegan *et al.* [33], the velocities measured as approximately 90% of the freestream velocity may be due to the non-zero sensitivity near the tunnel wall boundary layer edge. More study is needed to determine if (or to what extent) the FLDI measurement is influenced by the tunnel wall boundary layer.

E. Comparison with PCB Sensors

Two of the model sensors were located on the top ray of the cone (where the FLDI focused), both upstream (PCB19) and downstream (PCB20) of the FLDI beam spots. The locations of the PCB sensors and FLDI relative to each other (and to the base S1-S2 base seam of the cone model) was discussed in Section III.F (see Fig. 9a). The spectra from the two PCB sensors for Run 91 ($Re = 6.5 \times 10^6$ ft^{-1}) are studied relative to the two FLDI spectra to compare and contrast the two measurement methods. In Fig 22a, the top plot shows a zoom view of the unfiltered time series PCB data about a second-mode peak for both upstream (green) and downstream (magenta) sensors. In the bottom plot, the spectrogram of the same time series bounds is shown (for the downstream sensor only), with a peak near 350 kHz. In Fig. 22b, the spectra for the full time series PCB data are shown with lighter shades of green and magenta, while the spectra between the time bounds in Fig. 22a are shown with solid green and magenta lines for the upstream and downstream PCB sensors, respectively. The origin of the noisy broadband peak just above 10^5 Hz is unknown at this time, but may be a sensor-specific vibration and not a result of the physical flow. The distinct second-mode peak can be seen in the downstream data at 350 kHz, which then falls back down to the signal level of the upstream sensor for the all higher frequencies.

The time series data for both the FLDI and PCB signals are shown in Fig. 23a, where plots from top to bottom increase in distance downstream. The PCB and FLDI data are bandpass filtered near 330 kHz. The upstream PCB sensor does not have any clear second-mode packet signal. The middle two plots are the FLDI NP-pair beams, which both show a second-mode packet visible above the normal background disturbance levels. The downstream NP-pair beam is ≈ 2.47 mm downstream of the upstream NP-pair beam, and there is a slight delay in the signal from the packet in the upstream data to the downstream data, as is expected. The cross correlation between these two data sets gives the time lag of the signals, and thus a normalized phase speed of approximately 0.865. This value is notably below the mean normalized velocities discussed previously, but as seen in Fig. 21, values at this lower level do occur from time to time. The bottom plot shows the downstream PCB sensor time series, which also shows a second-mode packet similar to the FLDI system. The PCB sensor is approximately 15.5 mm downstream of the downstream FLDI NP-pair beam, and so the lag between the two signals is larger than the lag between the two FLDI signals. Note that the voltage levels of the FLDI and PCB data should not be compared.

The Welch spectra for the PCB and FLDI data can be seen in Fig. 23b, with colors matching those from the time series data. There is a clear second-mode peak near 330 kHz of the FLDI signals, with the downstream peak shifted to a slightly lower frequency in accordance with the increasing boundary layer thickness and lowering of the acoustic frequency of the trapped wave. A similar peak is seen in the downstream PCB sensor spectrum, with the peak shifted to an even lower frequency. A few more peaks are visible in the PCB spectrum, which may be harmonics developing from the packet as it grows in size.

A cross correlation method cannot be used between the FLDI and PCB data sets, so the lag time between packet

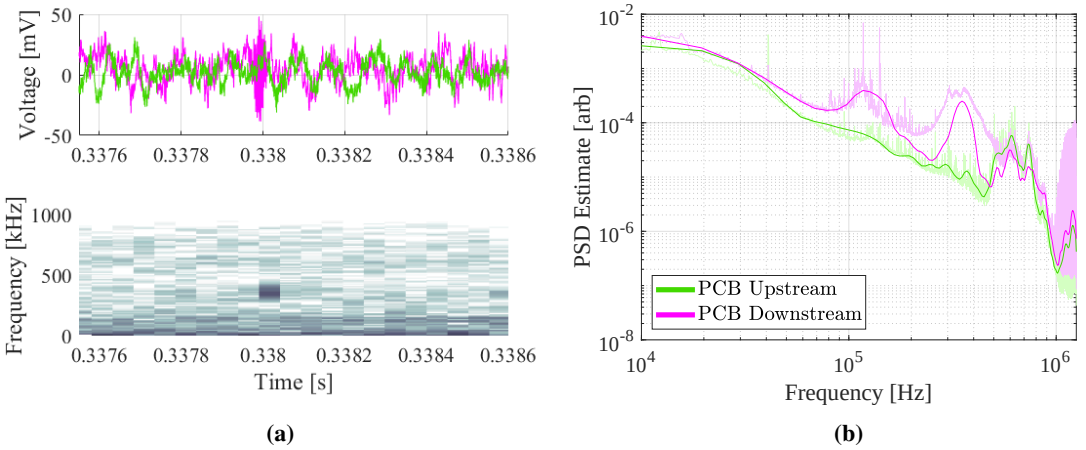

Fig. 22 Plots for (a) the time series data of both PCB sensors (top) and spectrogram for the downstream sensor (bottom), and (b) the spectrum of both upstream and downstream PCB sensors from the same time bounds shown in (a), along with full time series spectra in lighter shaded datasets. Darker shades on the spectrogram indicate larger values.

start times is used instead. Since the upstream PCB signal did not show the presence of a second-mode packet, the lag time is only computed between the downstream FLDI beam and downstream PCB sensor. The time lag is based on the difference in time between the start of the downstream FLDI packet and the start of the downstream PCB packet, and results in a normalized velocity of approximately 0.86. While this result agrees well with the normalized velocity of the FLDI data, there is a high uncertainty with these results for several reasons: the selection of the beginning time of the filtered packet is arbitrary based on the threshold voltage, the location of measurement for the FLDI beams (above the cone surface) and the PCB sensors (on the cone surface) are different, and the phase response of the PCB sensors to the actual second-mode packet is unknown.

VI. Conclusion

A two-point FLDI system was constructed for use in both laboratory measurements and for ground test facilities. The light weight, small footprint, and versatility of the system makes installation and alignment at facilities relatively quick. A polarizing Nomarski prism was used two split the normal single-point FLDI beam into two separate beams, which were used to determine velocities of density disturbances. The use of the Nomarski prism allows a single set of optics to be used, and provides rotation of the two beams about the optical axis of the system. The convergence angle of the Nomarski prism resulted in a separation of the distinct beams of 2.47 mm. The alignment procedure was described in detail, progressing from basic component layout to a full set of instructions for alignment of the pitch and catch breadboards. The alignment procedure that can be used when test section access is not available during tunnel testing was given in extensive detail, and could be accomplished with the use of a single CMOS camera on the catch breadboard.

To validate the disturbance velocity measurements from the two-point system, wave speeds from a laser induced breakdown spark were used. Nine different configurations of the NP-pair and W-pair orientations were used. High-speed schlieren (at 200 kHz) was used to validate the FLDI velocities, confirming that the system could be used with confidence for density disturbance velocity measurements in ground test facilities.

The system was installed at the 20-Inch Mach 6 air tunnel at NASA Langley, where both freestream data and boundary layer data on a 7 degree half-angle cone were measured over a testing campaign with 93 runs. The freestream data showed the precision of the FLDI system and the repeatability of the tunnel freestream frequency content distribution for different unit Reynolds numbers. For cone boundary layer measurements, four different flow types were identified, including background disturbances, second-mode packets, second-mode plus harmonic packets, and turbulent spots. An automated second-mode packet identification strategy was used to obtain the second-mode packet and turbulent spot rate as a function of unit Reynolds number. The second-mode packet rate first increased and then decreased for increasing unit Reynolds numbers. The turbulent spot rate increased with increasing unit Reynolds number, and its

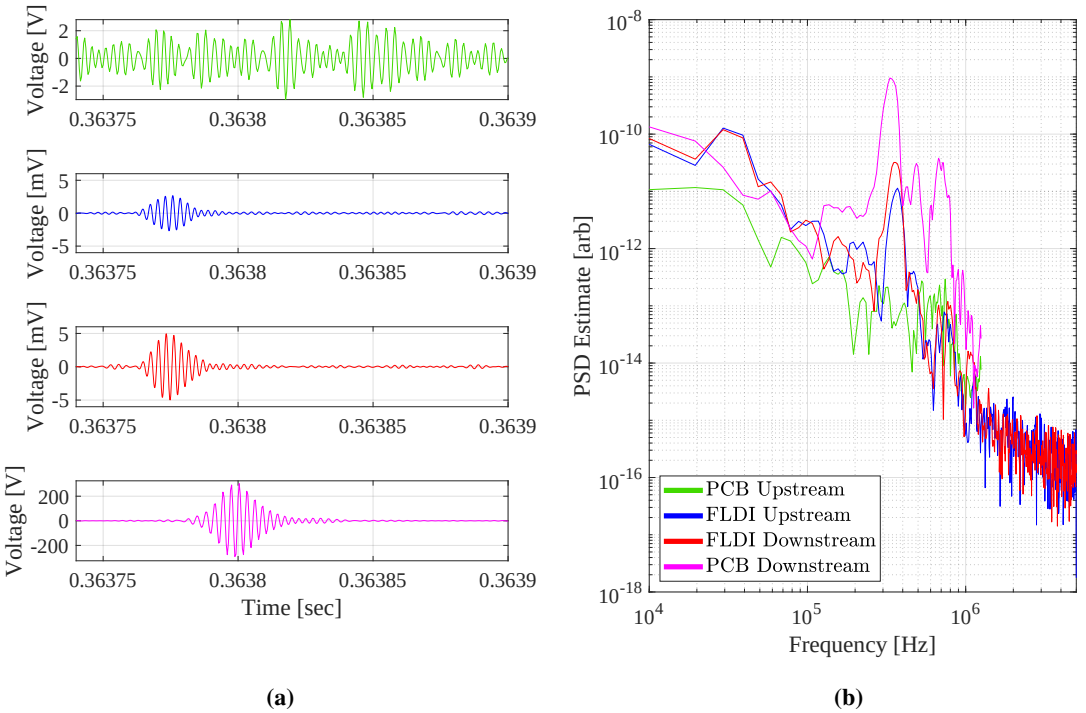

(a) (b)

Fig. 23 Plots of bandpass filtered (near 330 kHz) data of (a) the upstream PCB (green), upstream FLDI (blue), downstream FLDI (red), and downstream PCB (magenta) time series of a second-mode packet, and (b) the spectra for each corresponding time series data set.

slope grew larger at the same unit Reynolds number that the second-mode packet rate began to decrease.

Using both upstream and downstream FLDI measurement points (from the two-point system), the time lag between the two signals was found. Using the cross correlation of the narrow bandpass filtered signal about the second-mode peak frequency, the velocity of the packets normalized to the tunnel freestream velocity was calculated for each packet in the run. For all unit Reynolds numbers, this normalized velocity ranged from 0.88 to 0.92, with increasing values corresponding to decreasing unit Reynolds numbers.

Piezo-electric flush surface-mounted sensor data was also acquired during the runs, and two of these sensors bounded the FLDI measurement location (upstream and downstream). Second-mode packets were identified for the PCB data with the same method as the FLDI packet identification. Although a cross correlation between FLDI and PCB data could not be used, the time lag between both sets based on packet starting times resulted in normalized velocities that agreed well between both FLDI-FLDI data and FLDI-PCB data, albeit with high uncertainty.

Appendix

Alignment Without Test Section Access

Access to the test section at ground test facilities is not always practical, especially between runs on test days. Generally, access is only available before running for the day or after testing has been completed for the day. When access to the test section is available, the model will not always be able to be injected or available to be aligned to. A method for alignment without access to the test section must be used instead. The alignment process can be completed solely with the use of a CMOS camera on the catch board, placed at the same location as the prism mirror.

The PM-L5-L6 subsystem is first removed from the catch board. The camera is placed at the focus of the two NP-pair focusing beams; the sensor should be in the same location as the PM for this to be true. Note that the W^C is not necessarily in the correct position yet. The rotation of the W^C will be used to aid the alignment procedure, so first the behavior of the images with rotation of the W^C when knowing the orientation of the pitch optics is studied. In this case,

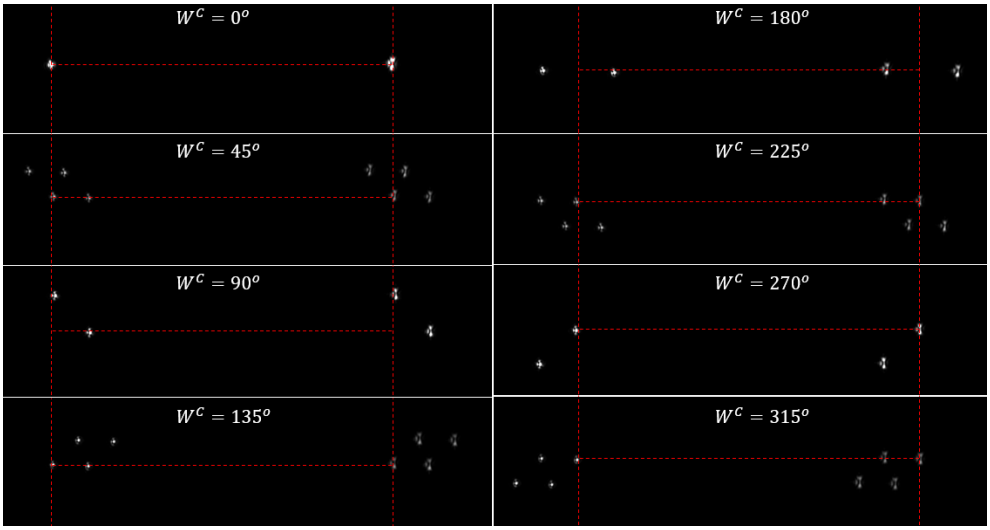

Fig. 24 Rotation of W^C in $45°$ increments, where $0°$ corresponds to the correctly balanced position of the W^C relative to the W^P. Red dashed horizontal and vertical lines are duplicated in each image from the $0°$.

the W-pair and NP-pair will both be aligned horizontal with respect to the breadboard. It is first assumed that the W^C is in the correct position to recombine the W-pair beams on the catch side, and this angle of W^C will be defined as $0°$. Without moving any components on the pitch side, the effect of rotating the W^C through one full rotation is shown in Fig. 24.

Fig. 25 First three steps of alignment procedure, with step 1 in red, step 2 in green, and step 3 in blue.

When both W^C and W^P are balanced, two spots are visible, each corresponding to one NP-pair beam (in this case they are horizontally aligned). The W^C is now rotated to its unbalanced states, starting with a $45°$ offset. At this angle, four beam spots are visible in each NP-pair. Looking at only the left NP-pair beam's four spots, top-two pair and the bottom-two pair are both horizontal, which is what the W-pair orientation is set to. The top two-pair and bottom two-pair are just two instances of the same W-pair, but since the W^C angle is unbalanced, a double instance is visible. Continuing the rotation offset to $90°$, the four spots have decreased to two, but not because of a the spots collapsing on itself. Instead, the unbalanced W-pair spots have disappeared due to the W^C alignment with respect to the incoming polarization. If the incoming polarization is aligned with, or offset by $90°$ with respect to, the fast axis of the W^C, then only the polarization aligned with the fast axis of the W^C will be transmitted. Recall that when aligning the HWP^{3P}, it was rotated such that the exiting polarization of each NP-pair beam was at $45°$ with respect to the W^P fast axis to produce two equal intensity W-pair beams. At the W^C $90°$ angle offset, one of the W-pair beams is blocked from passing through the W^C while the other is allowed to pass through. At an offset angle of $135°$, a state similar to the $45°$ case is seen. At $180°$ offset angle, two beams are visible in each NP-pair beam, aligned horizontally, but not recombined correctly as they are for the $0°$ balanced case. The next three $45°$ rotation increments are similar to the other states mentioned previously. At one full rotation, the balanced case of $0°$ is returned to, with only two distinct NP-pair beams visible. From these images in Fig.

24, two things are clear: the alignment of both the NP-pair and W-pair can be performed using a single camera on the catch board, and there is only one correct orientation of the W^C.

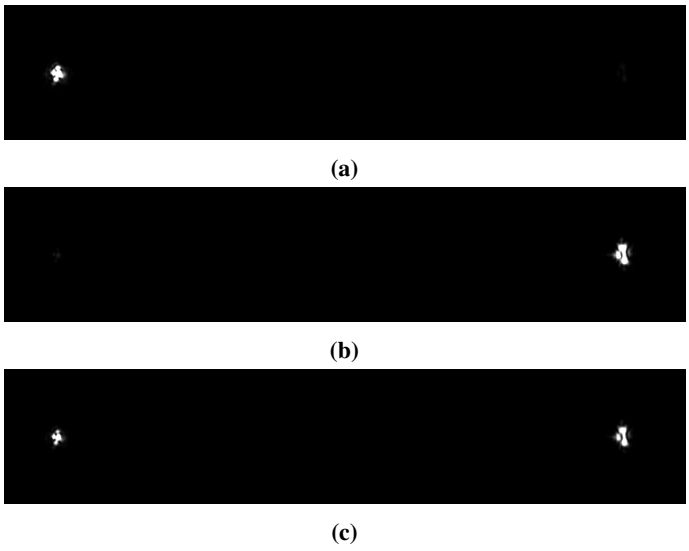

(a) **(b)** **(c)**

Fig. 26 Effect of rotating the HWP^{2P} to (a) 0°, (b) 45°, and (c) 22.5°.

Using information from the full rotation of the W^C, the alignment of a system of a system that has all components in incorrect and arbitrary initial orientations can be performed. The goal of this alignment test case is to return the alignment back to horizontal NP-pair and W-pair orientations. The first three steps in the process are shown in Fig. 25, where steps one through three are denoted with the color red, green, and blue, respectively. In the first step (red), all components are in arbitrary orientations. One NP-pair beam can be clearly seen to the bottom left (four points), and another NP-pair beam (with four points) can be very faintly seen at the top right. The NP-pair is not horizontal yet, and the intensity is also not balanced correctly. The W^C is clearly out of alignment for this orientation, since four spots are visible in each NP-pair beam cluster. For step two (green), the W^C is rotated such that the recombination of the W-pair beams is correct for the current NP-pair and W-pair orientations (neither of which is in the final orientation). Two spots are now visible, each corresponding to an NP-pair beam. It is again clear that the NP-pair is not horizontal, and also that the HWP^{2P} is not correctly oriented due to the difference in intensity of the two spots. For step three (blue), without moving the HWP^{2P}, the NP is rotated such that the NP-pair beams are horizontal. It appears that the intensities of the two are more similar now, since rotating the NP but not the HWP^{2P} may have made the splitting more equal.

To ensure the intensity splitting is equal between the two beams, the HWP^{2P} is now rotated in step four, as seen in Fig. 26. The HWP^{2P} angle is first set such that there is maximum signal on one beam and minimum signal on the other (Fir. 26a), and its angle is noted. The HWP^{2P} is then rotated such that the opposite condition is true (Fig. 26b), and the angle is noted. Balanced intensities of the beams is achieved by setting the HWP^{2P} to the middle of these two angles (Fig. 26c). The HWP^{2P} and NP can now be locked in place (until the fine-tune adjustment of the HWP^{2P} later with the detectors).

With the NP-pair aligned, the W-pair beams are now aligned. The W^C is still in the balanced position from earlier, so there is currently only a single beam spot visible for each NP-pair beam. First, the W^C is rotated ±45° (in either direction, see Fig. 27) from its balanced orientation. When rotating the W^P now, two of the spots in each of the four-spot clusters (for each NP-pair beam) will always rotate with each other, as shown in Fig. 28 for the left NP-pair beam only. The points that rotate together are the W-pairs, and when the W^C is unbalanced to ±45°, there will be two line pairs. In Fig. 28, the top two beam spots correspond to a single W-pair beam, and the bottom two beam spots correspond to another instance of that W-pair beam. The W^P is thus rotated until both instance of the W-pair beam spots is in the correct orientation (both instances will rotate at the same time, to the same orientation). Note that as the W^P is rotated, the individual spots in each W-pair beam instance will disappear and reappear because the HWP^{3P} is not being rotated at the same time. This can be seen faintly in Fig. 28 by looking at one W-pair beam instance. In the bottom instance, the left red spot is bright and the right red spot is dim. As the W^P is rotated, the left spot (now white) has decreased in intensity while the right spot has increased in intensity. When aligning the orientation of the W^P, the HWP^{3P} should be

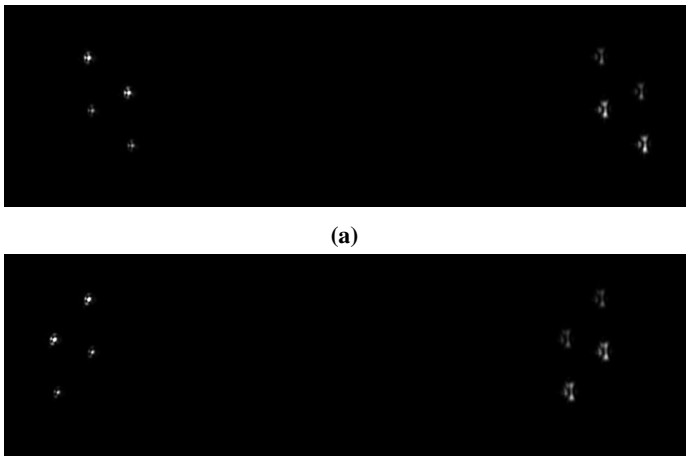

(a)

(b)

Fig. 27 Effect of rotating the W^C either (a) $+45°$ or (b) $-45°$ from its balanced position.

rotated enough to ensure both beam spots are visible.

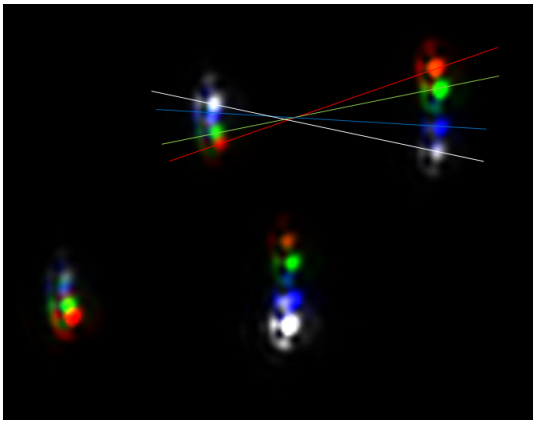

Fig. 28 Rotation of W^P showing W-pairs.

The W-pair beams are now aligned horizontally, as shown in Fig. 29a. By rotating the W^P, the balanced position of the W^C is no longer in the same orientation. To find the new balanced position, the W^C is rotated until only two points are visible, one for each NP-pair beam (Fig. 29b). The W^C needs to be unbalanced again to $\pm 45°$ in order to balanced the intensity of the W-pair beams, as shown in Fig. 29c, which may look similar to Fig. 29a, but is in fact a different orientation. If the W^C orientation from Fig. 29a is used for the HWP^{3P} balancing, the actual intensities between the W-pair beams will be incorrect.

To balance the intensity of the W-pair beams, the HWP^{3P} is rotated such that one W-pair instance (two spots in the four spot instance) is maximized and the other minimized, and the angle is noted. The HWP^{3P} is then rotated further until the opposite condition is found, and the angle is again noted. The balanced position of the HWP^{3P} is halfway between these two angles. To complete the alignment of the system, the W^C is rotated back by $\pm 45°$ to its balanced position at $0°$, and only the two NP-pair beams are visible on the camera.

Setup Difficulties and Solutions

The procedure for constructing and aligning the system to perform laboratory or tunnel testing has been outlined in detail in this study. However, there are still some minor difficulties and uncertainties in the process that are worth noting here.

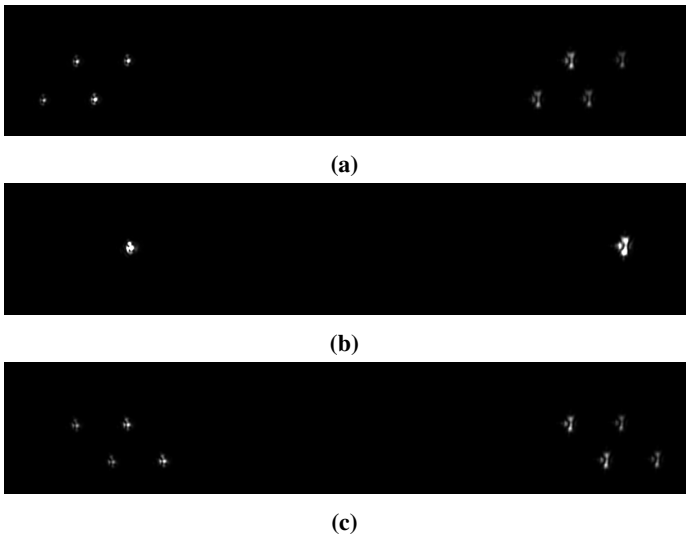

Fig. 29 Images of (a) W-pair beams aligned horizontal, (b) newly balanced W^C, and (c) the W^C unbalanced at ±45°.

1) The theoretical distances for the alignment along the optical axis of the position-sensitive components is simple to compute. These equations, however, do not take into account how the distances change with respect to addition of finite thickness optics. The NP is particularly difficult to account for because the crystal is 50.8 mm. As an example, if only the BE is in place (no NP, HWP^{3P}, and W^P), then the beam will expand and focus down from the FL^P to the theoretical beam spot, with the diameter dictated by the equation from earlier. After adding in the HWP^{3P} and the W^P, the beam spot size is different. The W-pair separation has also changed slightly. If it is not correct, then it is because the W^P is not at the effective focal length from the FL^P doublet. The same is true for adding the HWP^{2P} and NP into the system.
2) Aligning the NP-pair and W-pair to the desired angles can be complicated when simple vertical or horizontal orientations are not used. If using a CMOS camera to align the beam pairs, a level should be used to ensure the camera orientation is known precisely. If not, aligning the beam pairs to the horizontal or vertical camera axis would result in a systematic offset.
3) It is difficult to completely accurately define where the beam spots are in relation to the model. In earlier runs, the signal dropout near the beginning of the run time indicated how close the beams were to the model surface. However, as the oscillations decreased as the run time progressed, the signals were not cut out anymore, and it was hard to determine where in relation to the cone they finally settled out to.
4) To function ideally, the beam passing through the waveplate should be collimated. This is not always possible (actually very rarely in these compact setups), as they need to be located in the diverging or converging portion of the beam in most cases (except HWP^{1P} and HWP^{2P}). For a slowly diverging beam, the extra path length through the waveplate due to the off-axis nature of the beam will change the relative phase shift of the two orthogonal polarization components, but not appreciably, so these effects can be ignored for these measurements.
5) When aligning the HWP^{2P} to get the NP-pairs to have equal intensity, it is assumed that there is no clipping along the beam path all the way to the detectors for either beam. It is best to do this after finding the maximum signals on both detectors.
6) There are many places where beam clipping might occur: FL^C when BE, W^P, NP are not aligned properly, PM when not exactly centered on the cage system, and the $M^{\#C}$ adjustment of the laser focused onto the detector surface.

Acknowledgments

This work was supported by the NASA Hypersonic Technology Project (HTP) and the Transformational Tools and Technologies (TTT) project. The authors would like to thank Mark Kulick for his assistance in the fabrication of numerous hardware components that were used in this work, and Steffan Tesch for providing the PCB sensor

data. Support for this test was provided by facility technicians and engineers: Johnny Ellis, Grace Gleason, Kevin Hollingsworth, Larson Stacy, Sheila Wright, and Jonathan Crider.

References

[1] Schneider, S. P., "Hypersonic laminar-turbulent transition on circular cones and scramjet forebodies," *Progress in Aerospace Sciences*, Vol. 40, No. 1, 2004, pp. 1–50.

[2] Mack, L. M., "Linear Stability Theory and the Problem of Supersonic Boundary-Layer Transition," *AIAA Journal*, Vol. 13, No. 3, 1975, pp. 278–289. doi:10.2514/3.49693.

[3] Fedorov, A., and Tumin, A., "High-Speed Boundary-Layer Instability: Old Terminology and a New Framework," *AIAA Journal*, Vol. 49, No. 8, 2011, pp. 1647–1657. doi:10.2514/1.j050835.

[4] Laufer, J., "Aerodynamic Noise in Supersonic Wind Tunnels," *Journal of the Aerospace Sciences*, 1961.

[5] Demetriades, A., "Hypersonic viscous flow over a slender cone. III - Laminar instability and transition," No. 0 in Fluid Dynamics and Co-located Conferences, American Institute of Aeronautics and Astronautics, 1974. doi:10.2514/6.1974-535.

[6] Tanner, L. H., "The design of laser interferometers for use in fluid mechanics," *Journal of Scientific Instruments*, Vol. 43, 1966.

[7] Chou, A., Leidy, A. N., Bathel, B. F., King, R. A., and Herring, G. C., "Measurements of Freestream Fluctuations in the NASA Langley 20-Inch Mach 6 Tunnel," AIAA Aviation Forum, American Institute of Aeronautics and Astronautics, 2018.

[8] Heitmann, D., Radespiel, R., and Knauss, H., "Experimental Study of Boundary-Layer Response to Laser-Generated Disturbances at Mach 6," *Journal of Spacecraft and Rockets*, Vol. 50, No. 2, 2013, pp. 294–304. doi:10.2514/1.a32281.

[9] Casper, K. M., Beresh, S. J., and Schneider, S. P., "Pressure fluctuations beneath instability wavepackets and turbulent spots in a hypersonic boundary layer," *Journal of Fluid Mechanics*, Vol. 756, 2014, pp. 1058–1091. doi:10.1017/jfm.2014.475.

[10] Ort, D. J., and Dosch, J. J., "Influence of Mountiing on the Accuracy of Piezoelectric Pressure Measurements for Hypersonic Boundary Layer Transition," No. 0 in AIAA SciTech Forum, American Institute of Aeronautics and Astronautics, 2019. doi:10.2514/6.2019-2292.

[11] Smeets, G., "Laser-Interferometer Zur Messung An Achnellveranderlichen Schwachen Phasenobjekten," *Optics Communications*, 1970.

[12] Smeets, G., "Laser Interferometer for High Sensitivity Measurements on Transient Phase Objects," *IEEE Transactions on Aerospace and Electronic Systems*, Vol. AES-8, No. 2, 1972, pp. 186–190.

[13] Smeets, G., "Flow Diagnostics by Laser Interferometry," *IEEE Transactions on Aerospace and Electronic Systems*, 1977.

[14] Smeets, G., and George, A., "Laser-Differential Interferometer Applications in Gas Dynamics," Tech. rep., Intitut Franco-Allemand de Recherches Saint-Louis, 1996.

[15] Azzazy, M., Modarress, D., and Hall, R. M., "Optical Boundary-Layer Transition Detection in a Transonic Wind Tunnel," *AIAA Journal*, Vol. 27, No. 4, 1989, pp. 405–410. doi:10.2514/3.10127.

[16] Schmidt, B. E., and Shepherd, J. E., "Analysis of focused laser differential interferometry," *Applied Optics*, Vol. 54, No. 28, 2015, pp. 8459–8472.

[17] Settles, G. S., and Fulghum, M. R., "The Focusing Laser Differential Interferometer, an Instrument for Localized Turbulence Measurements in Refractive Flows," *Journal of Fluids Engineering*, Vol. 138, No. 10, 2016, pp. 101402–101402–10.

[18] Lawson, J. M., Neet, M. C., Grossman, I. J., and Austin, J. M., "Characterization of a Focused Laser Differential Interferometer," AIAA SciTech Forum, American Institute of Aeronautics and Astronautics, 2019. doi:10.2514/6.2019-2296.

[19] Parziale, N., Shepherd, J., and Hornung, H., "Reflected Shock Tunnel Noise Measurement by Focused Differential Interferometry," 42nd AIAA Fluid Dynamics Conference and Exhibit, American Institute of Aeronautics and Astronautics, 2012.

[20] Parziale, N. J., Shepherd, J. E., and Hornung, H. G., "Free-stream density perturbations in a reflected-shock tunnel," *Experiments in Fluids*, Vol. 55, No. 2, 2014, p. 1665.

[21] Parziale, N. J., Jewell, J. S., Leyva, I. A., and Shepherd, J. E., "Effects of Shock-Tube Cleanliness on Slender-Body Hypersonic Instability and Transition Studies at High Enthalpy," 53rd AIAA Aerospace Sciences Meeting, American Institute of Aeronautics and Astronautics, 2015.

[22] Jewell, J. S., Parziale, N. J., Leyva, I. A., and Shepherd, J. E., "Effects of Shock-Tube Cleanliness on Hypersonic Boundary Layer Transition at High Enthalpy," *AIAA Journal*, Vol. 55, No. 1, 2017, pp. 332–338. doi:10.2514/1.j054897.

[23] Harris, A. J., Kreth, P. A., Combs, C. S., and Schmisseur, J. D., "Laser Differential Interferometry and Schlieren as an Approach to Characterizing Freestream Disturbance Levels," AIAA SciTech Forum, American Institute of Aeronautics and Astronautics, 2018.

[24] Parziale, N. J., Shepher, J. E., and Hornung, H. G., "Differential Interferometric Measurement of Instability at Two Points in a Hypervelocity Boundary Layer," 51st AIAA Aerospac Sciences Meeting Including the New Horizons Forum and Aerospace Exposition, American Institute of Aeronautics and Astronautics, 2013.

[25] Parziale, N. J., Shepherd, J. E., and Hornung, H. G., "Differential Interferometric Measurement of Instability in a Hypervelocity Boundary Layer," *AIAA Journal*, Vol. 51, No. 3, 2013, pp. 750–754.

[26] Parziale, N. J., Shepherd, J. E., and Hornung, H. G., "Observations of hypervelocity boundary-layer instability," *Journal of Fluid Mechanics*, Vol. 781, 2015, pp. 87–112.

[27] Jewell, J. S., Parziale, N. J., Lam, K.-Y., Hagen, B. J., and Kimmel, R. L., "Disturbance and Phase Speed Measurements for Shock Tubes and Hypersonic Boundary-Layer Instability," 32nd AIAA Aerodynamic Measurement Technology and Ground Testing Conference, American Institute of Aeronautics and Astronautics, 2016.

[28] Ceruzzi, A., and Cadou, C. P., "Simultaneous Velocity and Density Gradient Measurements using Two-Point Focused Laser Differential Interferometry," No. 0 in AIAA SciTech Forum, American Institute of Aeronautics and Astronautics, 2019. doi:10.2514/6.2019-2295.

[29] Jewell, J. S., Hameed, A., Parziale, N. J., and Gogineni, S. P., "Disturbance Speed Measurements in a Circular Jet via Double Focused Laser Differential Interferometry," No. 0 in AIAA SciTech Forum, American Institute of Aeronautics and Astronautics, 2019. doi:10.2514/6.2019-2293.

[30] Parziale, N., "Slender-Body Hypervelocity Boundary-Layer Instability," Ph.D. thesis, California Institute of Technology, 05 2013.

[31] Shumway, N., and Laurence, S. J., "Methods for Identifying Key Features in Schlieren Images from Hypersonic Boundary-Layer Instability Experiments," AIAA SciTech Forum, American Institute of Aeronautics and Astronautics, 2015. doi: 10.2514/6.2015-1787.

[32] Hollis, B. R., "Real-Gas Flow Properties for NASA Langley Research Center Aerothermodynamic Facilities Complex Wind Tunnels," Tech. rep., NASA, 1996.

[33] Deegan, C. P., Duan, L., and Choudhari, M. M., "Direct Numerical Simulation of Acoustic Disturbances in the Rectangular Test Section of a Hypersonic Wind Tunnel," AIAA Aviation Forum, American Institute of Aeronautics and Astronautics, 2018.